Ore Geology Reviews 138 (2021) 104406

Contents lists available at ScienceDirect

Ore Geology Reviews

journal homepage: www.elsevier.com/locate/oregeorev

Magma evolution leading to veinlet-disseminated tungsten mineralization at the Muguayuan deposit: *In-situ* analysis of igneous minerals

Xiao-Yu Li [a], Jian-Jun Lu [a,*], Rong-Qing Zhang [a], Jian-Feng Gao [b,*], Jin-Wei Wu [a]

[a] State Key Laboratory for Mineral Deposits Research, School of Earth Sciences and Engineering, Nanjing University, Nanjing 210023, China
[b] State Key Laboratory of Ore Deposit Geochemistry, Institute of Geochemistry, Chinese Academy of Sciences, Guiyang 550081, China

ARTICLE INFO

Keywords:
In-situ analyses of minerals
Fluxing components
Scheelite mineralization
Sanxianba granite
South China

ABSTRACT

Whole rock geochemistry combined with spatially resolved geochemistry of zircon, apatite, biotite and plagioclase allows us to uncover the magmatic processes leading to ore formation at the Muguayuan deposit. The Sanxianba granite, associated with the Muguayuan veinlet-disseminated scheelite deposit, is located in the middle of the Jiangnan Orogen. Whole rock Sr and Nd isotopes, and zircon Lu-Hf isotopes suggest it might originate from the Neoproterozoic Banxi group strata. The Rb element modeling shows that, after ~35% of partial melting, the Banxi group metasandstone can generate the primary Sanxianba melt with 164 ppm Rb and 21 ppm W. The intra-/intercrystal texture and compositions of zircon and plagioclase indicate that W and other elements such as HREE, Th, U, Nb, Ta, and P increase in the melt during fractional crystallization. The water content in the early Sanxianba magma, calculated through the plagioclase-hydrometer, is ~4.4 wt%, and its enrichment in the melt is reflected by the increasing water content in biotite with fractionation. F content in the early apatite is relatively high and invariable but further elevated in the late apatite. Chlorine, LREE and Na contents in the early apatite also present an enrichment trend. When H_2O and Cl start to be saturated with the magma fractionation in the deep magma chamber, Cl-, Na-, and LREE-rich but W-poor fluid exsolves from the melt, resulting in the albitization and chloritization of feldspar and biotite phenocrysts, respectively. The subsequent decrease of Cl, Na_2O and La_2O_3 in the late apatite record this first fluid exsolution. Fluorine, P, H_2O and W continue to enrich in the evolved melt with fractionation after the Cl-rich fluid exsolution. These fluxing components reach oversaturation during the shallow-ward emplacement of the magma, forming the F-, P- and W-rich fluids. The apex of the intrusion cools and forms a solid barrier, which prevents the escape of fluids. The exsolved fluids from the underlying magma continuously supply upward and react with the apex along fractures, resulting in greisenization and phyllic alteration. During alteration, Ca is released from calcium-rich plagioclase and combines with tungsten in the fluids to form scheelite mineralization. Magma evolution leading to the tungsten mineralization may be also the general scenarios in the other granite-related veinlet-disseminated scheelite deposits.

1. Introduction

Magmatic-hydrothermal tungsten deposits are the primary sources for tungsten. They typically exhibit a spatial and temporal association with shallow, porphyritic or variably textured intrusions with relatively highly fractionated compositions, and a wealth of evidence has revealed that ore-forming fluids and tungsten are derived from these intrusions during magma degassing (Černý et al., 2005; Linnen and Cuney, 2005; Mao et al., 2013; Pirajno, 2009; Zhao et al., 2017a; 2017b). Tungsten belongs to high-field-strength elements (HFSE), and is concentrated in residual melt during magma differentiation (Černý et al., 2005; Linnen and Cuney, 2005). Volatiles (like H_2O and F) are also highly incompatible during magma fractionation (London, 1997; Pyle and Mather, 2009; Webster et al., 2004). Once over-saturated, fluids exsolve and sequester the tungsten from the evolved melt (Audétat et al., 2000, Keppler and Wyllie 1991; Zajacz et al. 2008), forming magmatic-hydrothermal tungsten deposits (Audétat et al., 2000; Hedenquist and Lowenstern, 1994; Pirajno, 2009 and reference therein). Hence, volatiles and tungsten enrichment during the fractionation of ore-bearing granite is vital for tungsten mineralization (c.f. Audétat et al., 2000;

* Corresponding authors.
E-mail addresses: lujj@nju.edu.cn (J.-J. Lu), gaojianfeng@mail.gyig.ac.cn (J.-F. Gao).

https://doi.org/10.1016/j.oregeorev.2021.104406
Received 22 January 2021; Received in revised form 1 August 2021; Accepted 7 August 2021
Available online 13 August 2021

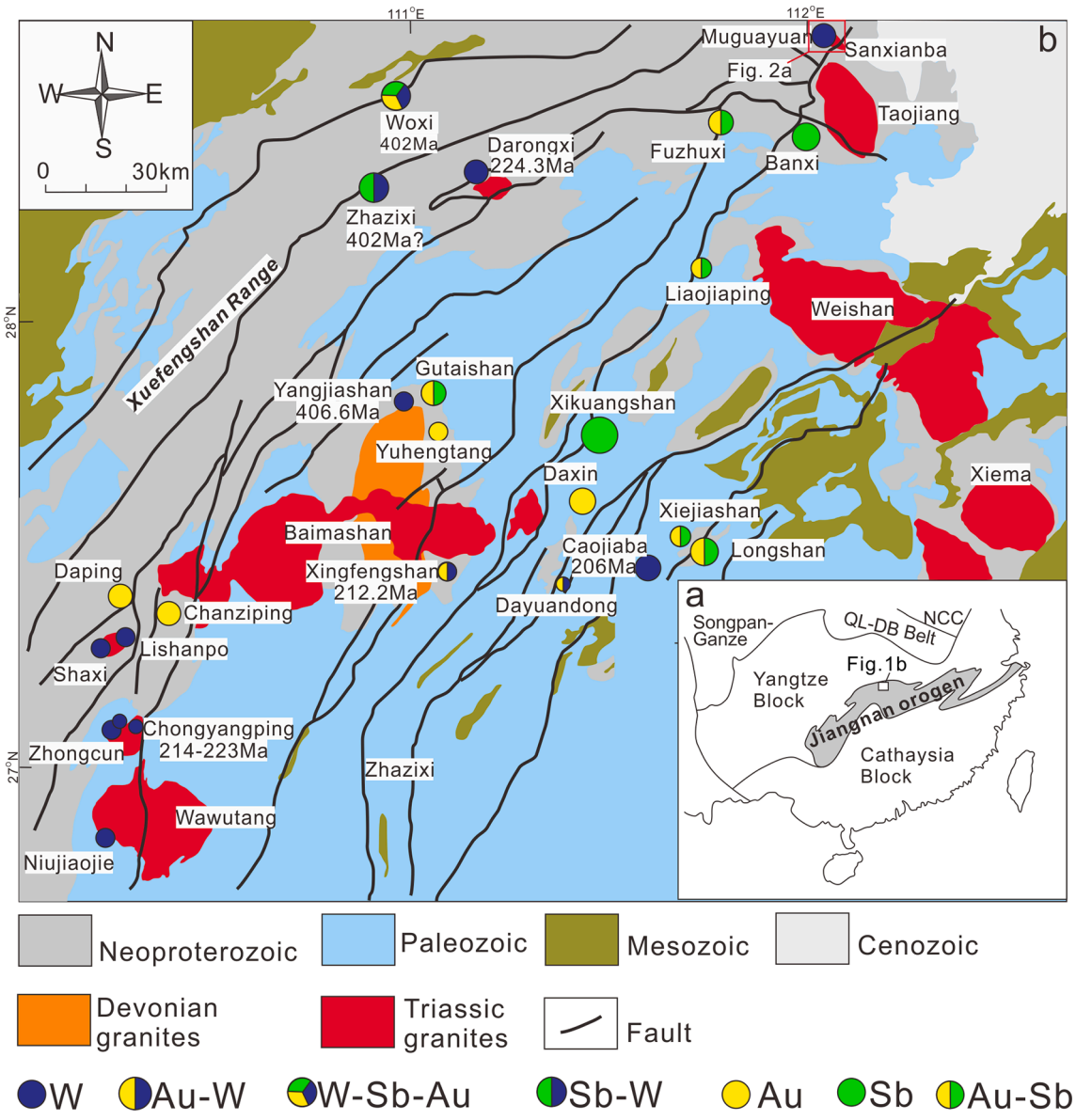

Fig. 1. The regional geological map of the Central Hunan Metallogenic Province (CHMP) in the middle of the Jiangnan Orogen (JNO), South China (modified after Xie et al., 2018a). Inset a shows tectonic framework of JNO including the location of CHMP.

Manning and Hill, 1990; Pollard et al., 1987; Webster et al., 2004). Due to the elusive behavior of volatiles and tungsten during the magmatic and magmatic-hydrothermal evolution, whole rock geochemistry usually fails to give the detailed record (c.f. London, 1997). Melt inclusions may provide important constraint on the evolution of volatiles and W during the fractionation of the magma (c.f. Audétat et al., 2000; Audétat, 2019; Webster et al., 2004). However, these studies are restricted by the accessibility, developmental and preservation situation, as well as representativeness of inclusions (c.f. Portnyagin et al., 2008; Wilkinson, 2001). The volatiles and tungsten enrichment trend during the fractionation of magma can be recorded by the compositions of the coexistent minerals (c.f. Berni et al., 2017; London, 1997). In recent decades, accurate *in-situ* composition analysis and high-resolution electronic imaging of minerals have made great progress (Brugger et al., 2000, 2008; Zhang et al., 2018), which makes it possible to decipher the volatile and tungsten enrichment process during magmatic and magmatic-hydrothermal fractionation (c.f. Berni et al., 2017; Breiter et al., 1997; Li et al., 2015). Mica and apatite are the main hydrous minerals in granite, and can provide solid constraints on the budget of volatiles and their evolution in granite (c.f. Rasmussen and Mortensen, 2013; Zhang et al., 2016). Trace elements of mica can also serve as diagnostic fertility indexes of tungsten for granite (c.f. Azadbakht et al., 2020). Zircon is a refractory mineral that can resist alteration during the metasomatism of the rock, which make it a powerful tracer for the evolution of magma (c.f. Large et al., 2018) and diagnostic fertility index of ore elements in granite (c.f. Nie et al., 2020). Combining high-resolution electronic imaging with accurate *in-situ* compositional analysis of these minerals, one can uncover the volatiles and tungsten enrichment process during the magmatic and magmatic-hydrothermal fractionation.

Veinlet–disseminated scheelite deposits occur mainly in granitic rocks and have previously been considered to be sub-economic (Seedorff et al., 2005; Sinclair et al., 2011). However, in the past decade, several large veinlet–disseminated scheelite deposits, such as the giant Dahutang, and the large Dongyuan tungsten deposits, have been discovered in the Jiangnan Orogen, South China (Huang and Jiang, 2014; Wang et al., 2017), making it one of the most important tungsten metallogenic belts in the world. Some pioneering studies on granite petrogenesis (Huang and Jiang, 2014; Mao et al., 2017), fluid origin (Wang et al., 2017; Sun

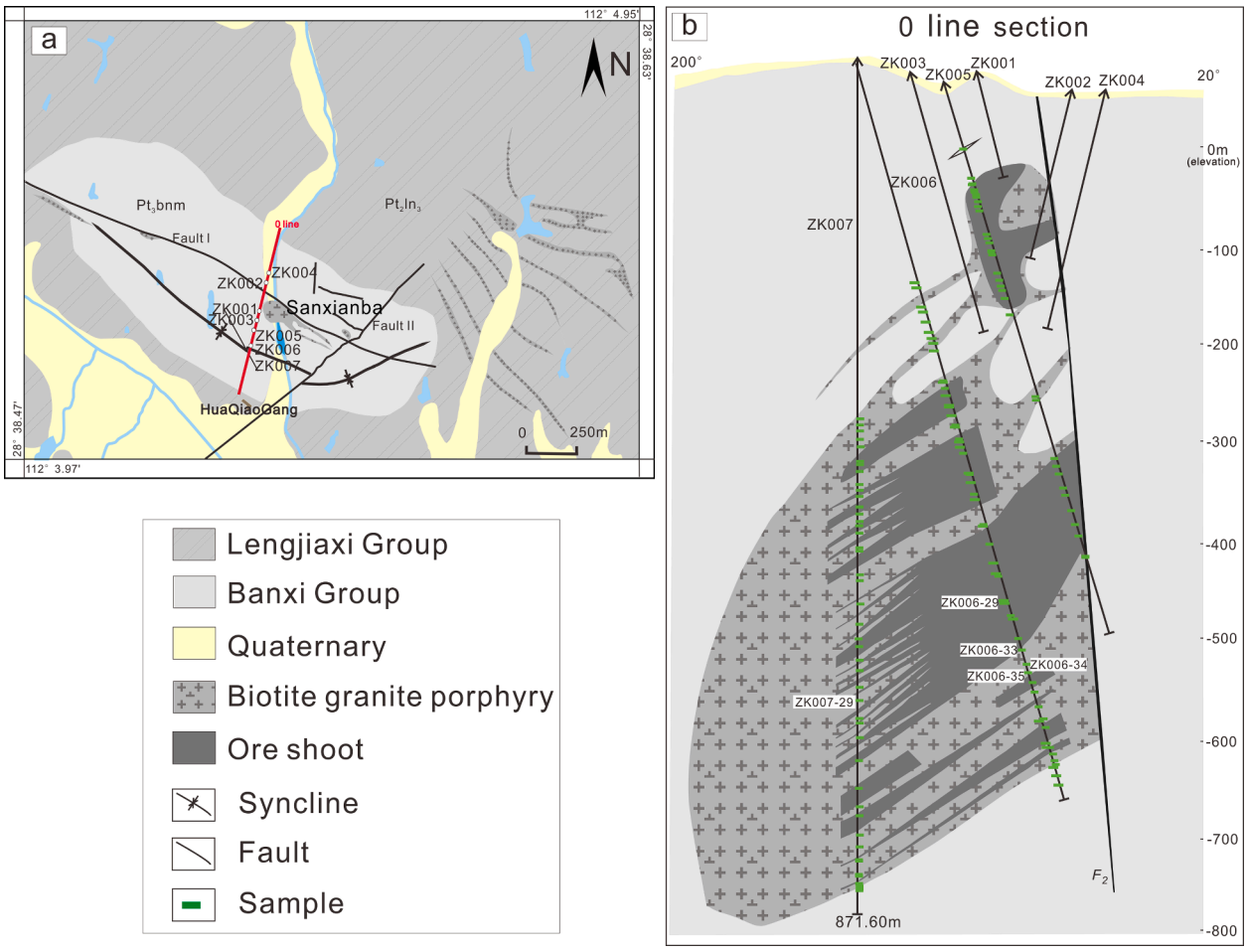

Fig. 2. Geological sketch map of the Muguayuan W deposit (a) and the 0 line drill section profile (b) (modified after No. 418 Geological Team, unpublished report and Li et al., 2018). In b, the samples selected to conduct whole rock and in-situ mineral analysis are specially labeled with their numbers.

and Chen, 2017) and mineralization process (Li et al., 2018) of these deposits have been conducted. However, the enrichment process of volatiles and tungsten during the magma fractionation are still poorly understood.

The Muguayuan deposit located in the middle Jiangnan Orogen is a typical veinlet-disseminated scheelite deposit (Li et al., 2018). The tungsten mineralization in the Muguayuan is associated with the Sanxianba granite and related to alteration within the Sanxianba granite. Ore minerals are dominant by scheelite with minor wolframite and molybdenite in the Muguayuan deposits. Previous studies on ore geology, geochronology, and in-situ composition of scheelite of the Muguayuan deposit have been conducted (Li et al., 2018; Luo and Shu, 2017; Shan et al., 2019; Tang et al., 2016), and the timing of magmatism and mineralization, evolution processes of ore-forming fluids have been preliminarily understood. However, the genesis and evolution of the ore-forming granite, especially the enrichment process of volatiles and tungsten during the magma evolution, are still poorly constrained. In this study, we conduct *in-situ* U-Pb dating and Lu-Hf isotopes analysis on zircon and *in-situ* composition analysis of plagioclase, biotite, zircon, and apatite, combined with trace element modeling, to constrain the volatile and tungsten enrichment process during the magma evolution and its role for tungsten mineralization in the Sanxianba granite.

2. Geological background

The Jiangnan Orogen (JNO) is located between the northwest Yangtze Block and the southeast Cathaysia Block (Fig. 1a). The strata in the JNO mainly comprise pre-Sinian rocks, interpreted as the basement to the southeast Yangtze Block, and a cover sequence of Sinian (0.8–0.57 Ga) and post-Sinian sedimentary strata of neritic and terrestrial facies (c.f. Wang et al., 2004, 2007; Xu et al., 2007). Since the Neoproterozoic, multi-stage granitic magmatism and related W(-Sn) mineralization took place in the JNO (Chen, 2016; Huang and Jiang, 2014; Xie et al., 2018a, b; Zhang et al., 2019), forming the world-class Jiangnan Orogen tungsten metallogenic belt (Mao et al., 2019).

The basement in the middle of JNO consists of Neoproterozoic clastic metasediments and volcanic rocks of the Lengjiaxi and Banxi Groups (Fig. 1b, Wang et al., 2007a; Xu et al., 2007). The granitoids in this district are mainly biotite monzogranite/granodiorite and biotite granite with subordinate two-mica or muscovite granite (Chu et al., 2012; Wang et al., 2007b). These granitoids are mainly late Triassic, with a few early Devonian (Fig. 1b; Chu et al., 2012; Xie et al., 2018b). Many veinlet-disseminated, skarn scheelite and quartz vein deposits are spatially and/or genetically related to these granitic rocks (Xie et al., 2018a, b; Zhang, 2013).

The Muguayuan veinlet-disseminated scheelite deposit is hosted in the Sanxianba granite stock with a resource of 25,300 t WO_3 grading 0.12 wt% (Tang et al. 2016; Luo and Shu 2017). The Sanxianba stock, with the total outcrop area of around 200 m^2, was emplaced near the axis of the Huaqiaogang syncline (Fig. 2a). Several contemporary granite porphyry dikes outcrop to the east of the stock (Fig. 2a), but do not show any ore mineralization associated with them (No. 418 Geological Team, unpublished report). Drill cores show that the underground portion of the Sanxianba stock has a faulted wall rock contact (F2) to the north–north-east, but the extension to the south-south-west is unclear (Fig. 2b). The outcrop portion is intensely weathered, and the

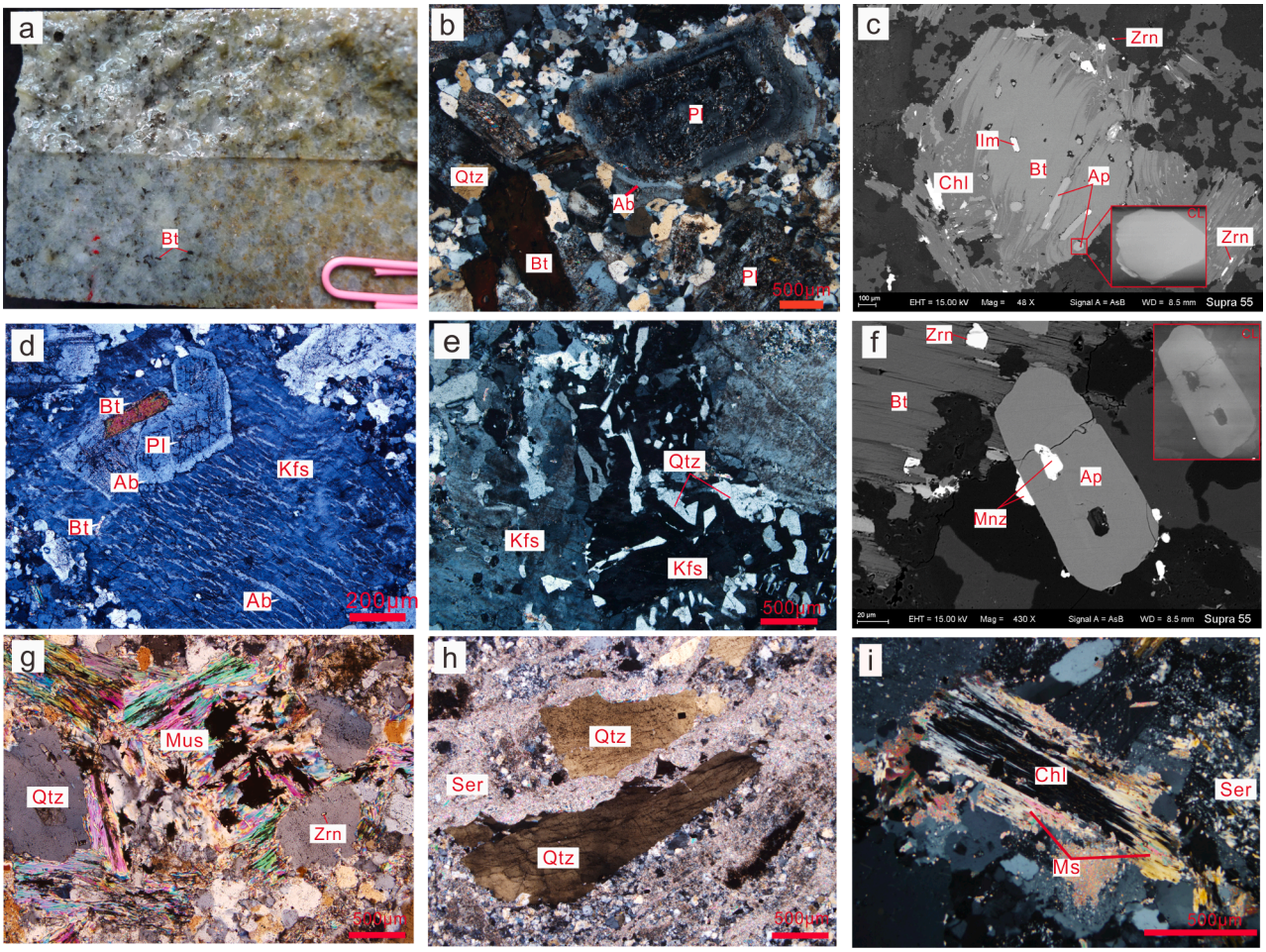

Fig. 3. The mesoscopic images of the representative hand samples (a), and photomicrographs and BSE images showing the petrography (b-i) of the Sanxianba stock. In which d and g are modified after Li et al.(2018). **a:** Biotite-bearing granite porphyry. The right is overprinted by alteration. ZK007-24, −530 m deep. **b:** Porphyritic texture. The plagioclase phenocryst is euhedral and zoned, with a hydrothermal albite overgrowth rim. ZK007-24, −530 m deep. **c:** Biotite phenocryst rim is replaced by chlorite. Relatively small-grained euhedral apatite (Ap-earlier) and zircon are included in the biotite phenocryst. There is also zircon grain in the matrix. ZK007-29, −570 m deep. **d:** The paragenesis of biotite, plagioclase and K-feldspar. Biotite is hosted by the plagioclase, and they both are enveloped by K-feldspar. K-feldspar are altered by albite veinlet. ZK007-4, −300 m deep. **e:** Quartz and K-feldspar are in characteristic angular intergrowths to form granophyric texture. ZK005-04, −20 m deep. **f:** Apatite, associated with monazite, occurs as isolated crystal in the matrix. ZK006-35, −540 m deep. **g:** Greisenization consumes nearly all rock-forming minerals. **h:** Phyllic alteration in which sericite replaced all early minerals. **i:** Biotite is replaced by chlorite firstly and the latter is replaced by muscovite from rim during greisenization. Insets in the (c) and (f) are CL images of apatite. Ab: albite, Ap: apatite, Bt: biotite, Chl: chlorite, Kfs: K-feldspar, Ilm: ilmenite, Mnz: monazite, Pl: plagioclase, Qtz: quartz, Zrn: zircon.

underground part shows various degree of alteration. Scheelite mineralization is closely related with alteration in the Sanxianba granite, and major stages of mineralization and veining are identified at the Muguayuan (Li et al., 2018) as follows: Pre-ore albitization and chloritization; stage I disseminated-veinlet scheelite mineralization consisting of scheelite ± wolframite ± molybdenite ± pyrite ± arsenopyrite ± rutile and quartz + muscovite ± apatite ± ankerite; stage II veinlet scheelite mineralization composed of scheelite ± pyrite ± arsenopyrite and quartz + sericite ± apatite ± ankerite; post-ore sulfide (pyrite ± galena ± sphalerite) and quartz + calcite ± pyrite veinlets.

3. Sampling and analytical methods

Hand specimens were collected from three drill holes (ZK005, ZK006, and ZK007, Fig. 2b). After systematic core cataloging and petrographic observation, we found no further intrusions or sharp lithological change in the Sanxianba stock (see below). ZK006-35 and ZK007-29 are the least-altered, and hold the primary structure and mineral assemblage of the Sanxianba granite to the greatest extent, thus we selected them to conduct whole rock geochemistry and Sr and Nd isotope analyses. Polished thin sections for samples ZK006-29, ZK006-33, ZK006-34, ZK006-35 and ZK007-29 were prepared to conduct scanning electron microscopy (SEM) observation and *in-situ* mineral analysis. Zircon grains were separated from ZK006-35 using conventional techniques of density and magnetic separation. Representative zircon grains were handpicked under a binocular microscope, mounted in epoxy resin, and polished, so as to conduct microscope observation and *in-situ* analyses. Cathodoluminescence (CL) images of zircon and apatite were taken using a Carl Zeiss Supra 55 field-emission scanning electron microscope (FE-SEM) coupled to a GATAN MonoCL4 detector at the State Key Laboratory for Mineral Deposits Research in Nanjing University, China.

Major element analysis of whole rock was carried out through wet chemistry methods at the Analysis Center of No. 230 Research Institute of the China National Nuclear Corporation, Changsha, following the procedures described in the China National Standards GB/T 14506.3-2010–GB/T14506.14-2010. The analytical precision for all elements was better than ±5%. Trace elements and rare earth element analysis of whole rock were carried out at the FocuMS Laboratory (Nanjing, China) using the Agilent Technologies *7700x* quadrupole ICP-MS (Hachioji,

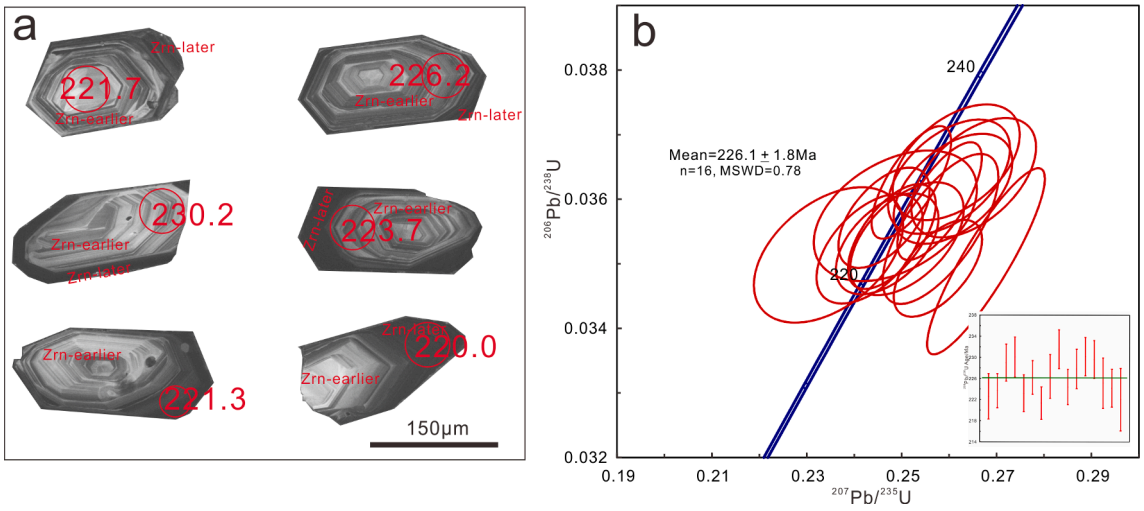

Fig. 4. The cathodoluminescence (a) and U-Pb age (b) of zircons from the Sanxianba granite. The red circles and numbers on the zircons in (a) represent the analyzed spots and corresponding U-Pb ages (in Ma), respectively. (For interpretation of the references to colour in this figure legend, the reader is referred to the web version of this article.)

Table 1
Whole rock geochemistry and Sr and Nd isotopes compositions of the Sanxianba granite.

Sample		SiO_2	TiO_2	Al_2O_3	Fe_2O_3	FeO	MnO	MgO	CaO	Na_2O	K_2O	P_2O_5	H_2O	LOI	Total	ASI	CIA
ZK006-35	wt. %	71.80	0.33	13.73	0.57	1.79	0.04	1.11	1.83	2.79	4.14	0.09	0.53	0.89	99.62	1.11	52.54
ZK007-29		71.14	0.32	14.22	1.44	1.19	0.04	1.07	1.98	3.04	4.00	0.10	0.42	0.75	99.69	1.10	52.37

	F	Cl	Li	Ga	Rb	Sr	Y	Zr	Nb	Sn	Ba	La	Ce	Pr	Nd	Sm
ppm	1030	52.2	58.2	18.6	193	138	18.1	159	8.97	4.43	493	37.0	71.1	7.65	26.1	4.65
	1070	48.6	63.1	19.2	183	166	18.1	127	8.32	3.56	532	41.4	78.2	8.39	28.7	4.95

Eu	Gd	Tb	Dy	Ho	Er	Tm	Yb	Lu	Hf	W	Ta	Th	U	Zr/Hf	Th/U	Nb/Ta	Tzr(℃)
0.702	3.82	0.585	3.28	0.649	1.83	0.269	1.72	0.252	4.75	45.0	0.990	22.6	5.93	33.47	3.81	9.06	809
0.781	3.97	0.594	3.21	0.619	1.76	0.255	1.61	0.231	3.77	69.7	0.787	24.0	4.09	33.68	5.87	10.57	791

$^{87}Sr/^{86}Sr$	1 Std Error	$^{87}Rb/^{86}Sr$	$(^{87}Sr/^{86}Sr)i$	$^{143}Nd/^{144}Nd$	1Std Error	$^{147}Sm/^{144}Nd$	$(^{143}Nd/^{144}Nd)i$	εNd(226)	T_{DM} (Ma)	T_{2DM} (Ma)
0.731138	0.000004	4.053177947	0.718363196	0.512055	0.000002	0.107694	0.511899	−8.85	1574	1719
0.729154	0.000004	3.201509501	0.719064179	0.512064	0.000002	0.104352	0.511913	−8.58	1513	1697

Tokyo, Japan). Deviation was better than ±10% for the elements exceeding 10 ppm and better than ±5% for the elements exceeding 50 ppm. Strontium and neodymium isotope compositions were measured at the FocuMS Laboratory (Nanjing, China) using Nu Plasma II MC-ICP-MS (Wrexham, Wales, UK) through Teledyne Cetac Technologies Aridus II desolvating nebulizer system (Omaha, Nebraska, USA). The sample preparation and isotope analysis procedure followed the description of Muhtar et al. (2020).

Zircon U-Pb and Lu-Hf isotopes were analyzed at the FocuMS Laboratory (Nanjing, China) using the Teledyne Cetac Technologies Analyte Excite laser-ablation system (Bozeman, Montana, USA) coupled with an Agilent Technologies 7700x ICP-MS (Hachioji, Tokyo, Japan) and the Australian Scientific Instruments RESOlution LR laser-ablation system (Canberra, Australian) attached to Nu Instruments Nu Plasma II MC-ICP-MS (Wrexham, Wales, UK), respectively. The analysis procedure is similar to the methods of Cong et al. (2019).

Electron microprobe analysis (EMPA) on feldspar, biotite, and apatite were conducted using a JEOL JXA-8100 microprobe at the State Key Laboratory for Mineral Deposits Research at Nanjing University, China. The standard sets for feldspar and mica are same as Huang and Jiang (2014), and for apatite are same as Li et al. (2015). All data were corrected with standard ZAF correction procedures. *In-situ* compositions of biotite and zircon were measured with a Photon Machines Excite 193 nm laser ablation system coupled to an Agilent 7700x ICP-MS at the FocuMS Laboratory, Nanjing, China. The details of measurement are similar with the description in Li et al. (2018).

4. Results

4.1. Petrology of the Sanxianba stock

Careful core cataloging and petrographic observation have been conducted for the collected samples. The Sanxianba stock is composed of single phase of biotite granite porphyry (Fig. 3a) without other intrusion sequence in the stock. The 0 line drill section (Fig. 2) is taken as the window to describe the main petrologic characteristics of the Sanxianba stock. The phenocrysts in the stock mainly comprise plagioclase (20–30 vol%), K-feldspar (30–40 vol%), quartz (30–40 vol%), and biotite (~5 vol%) (Fig. 3b-e), and the groundmass is mainly quartz and feldspar. Plagioclase phenocrysts are euhedral, with a zoned texture (Fig. 3b). Biotite phenocrysts are flaky with ragged edges (Fig. 3c). Sometimes, the relatively fresh biotite is hosted in the plagioclase, and they both are enveloped by K-feldspar (Fig. 3d). Quartz is subhedral, sometimes with embayed rims. Near the intrusion margin, quartz and K-feldspar can be in characteristic angular intergrowths to form granophyric texture (Fig. 3e). The accessory minerals mainly include zircon, apatite, ilmenite, and monazite (Fig. 3c, f). Apatite occurs as mineral inclusions (Ap-earlier) in biotite phenocryst (Fig. 3c), or isolated euhedral grains (Ap-later) in the groundmass (Fig. 3f). The Ap-earlier occurs as small euhedral crystal with no mineral inclusion, while the Ap-later is

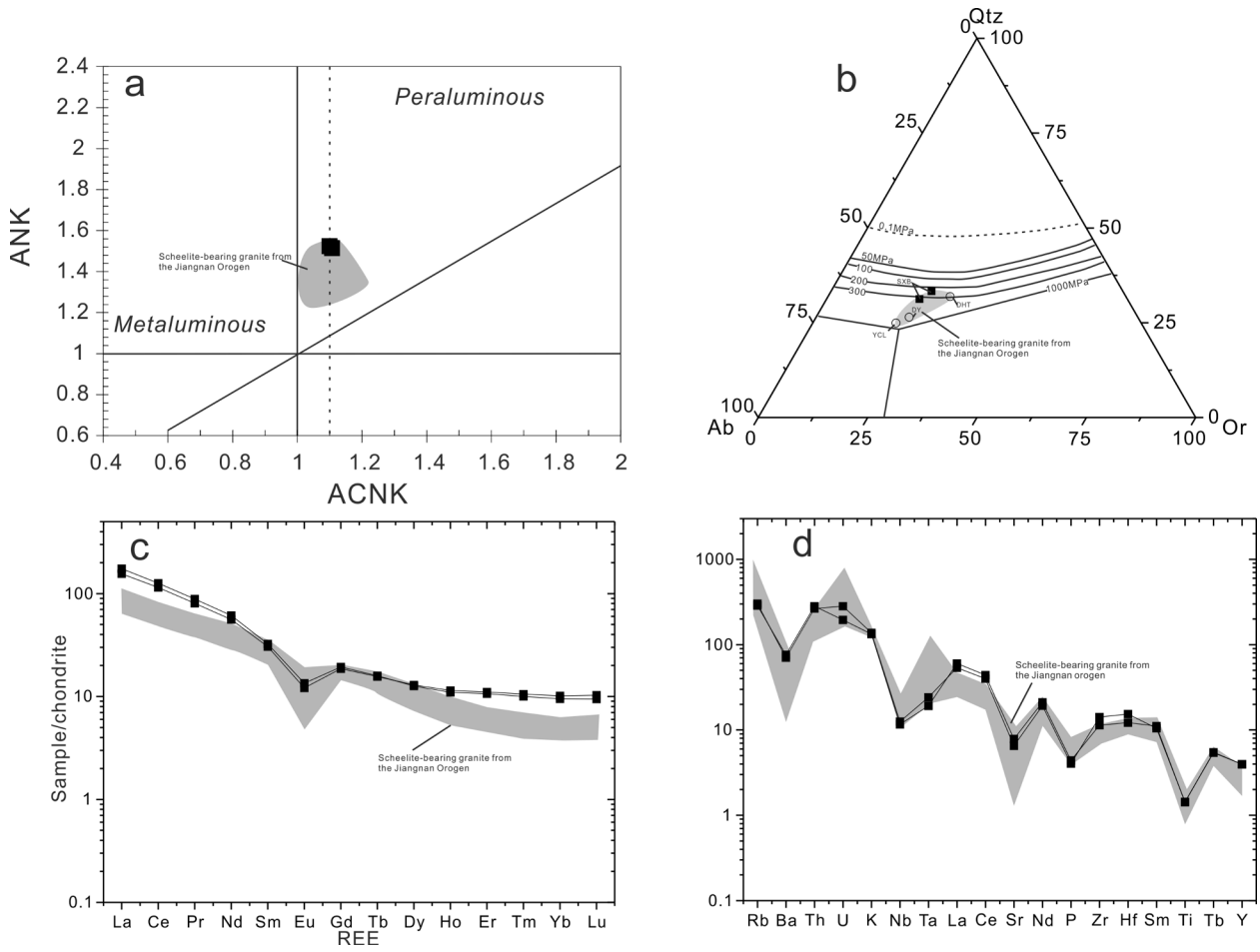

Fig. 5. Major and trace elements of the Sanxianba granite. **a:** ACNK vs. ANK. **b:** Projection of quartz (Qtz), albite (Ab), and orthoclase (Or) contents of the Sanxianba granite (SXB, this study), the Yangchuling granite (YCL, Mao et al., 2017), the Dongyuan granite (DY, Wang et al., 2007b), the Dahutang granite (DHT, Huang and Jiang, 2014) onto the Qz-Ab-Or ternary (after Blundy and Cashman, 2001). **c:** Chondrite-normalized REE pattern of the Sanxianba granite. **d:** Primitive mantle-normalized trace element of the Sanxianba granite. Chondrite and primitive mantle compositions are from Sun and Mcdonough (1989). The data range for scheelite-bearing granite from the Jiangnan Orogen is according to Huang and Jiang (2014), Wang et al. (2007b) and Mao et al. (2017).

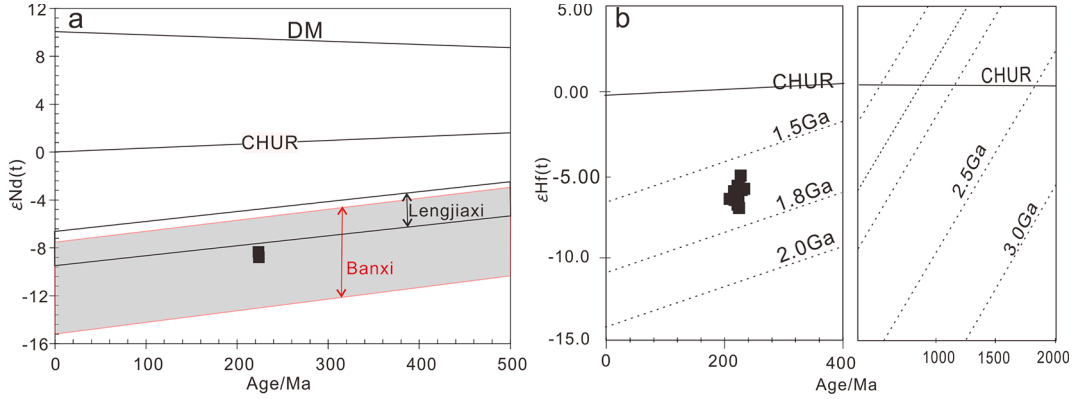

Fig. 6. Whole rock Sr, Nd, and *in-situ* zircon Hf isotopic compositions of the Sanxianba granite. **a:** εNd(t)-t(Ma) diagram, the Nd isotopic evolution region of the Neoproterozoic basement of the district are outlined according to the data of Li and McCulloch (1996) and Wang et al. (2010). **b:** εHf(t)-t(Ma) diagram.

relatively larger than Ap-earlier and may envelope felsic mineral inclusions (Fig. 3f). Under CL, the apatite are relatively homogeneous, without obvious textural and/or compositional zoning (insets in Fig. 3c, f). A few anhedral monazites are associated with apatite in the groundmass (Fig. 3f). Zircons are transparent prismatic crystals and disseminated in the Sanxianba stock, as inclusions in phenocrysts (e.g. biotite) and/or isolated grains in groundmass (Fig. 3c, f, g). The alteration types are mainly albitization, chloritization, greisenization, and phyllic alteration (Fig. 3g-i). The former two are usually constrained to the feldspar and biotite phenocrysts, respectively (Fig. 3b-d). The latter two are widespread and overprint the albitization and chloritization (Fig. 3g-i).

Table 2
EPM compositions (in wt. %) for the feldspar from the Sanxianba granite.

Sample	ZK006-33										ZK006-29					
	phenocryst										phenocryst			phenocryst		
Spot No.	1	2	3	4	5	6	7	8	9	10	19	20	21	11	12	13
SiO_2	53.89	58.49	59.73	58.42	59.07	58.72	58.88	57.17	58.02	54.91	59.69	58.90	58.63	64.26	63.40	62.91
TiO_2	b.d.	0.07	0.05	0.02	0.03	0.08	0.03	0.02	b.d.	0.09	0.05	0.01	0.03	b.d.	0.04	b.d.
Al_2O_3	28.96	26.65	26.19	26.94	25.59	27.12	26.68	26.52	25.63	28.83	26.84	26.09	26.02	18.66	18.23	18.24
FeO	0.07	0.09	0.08	0.09	0.10	0.05	0.09	0.08	0.08	0.12	0.09	0.07	0.07	0.07	0.03	0.06
MnO	0.03	b.d.	0.03	0.02	b.d.	b.d.	0.00	0.01	0.01	b.d.	b.d.	0.02	0.02	0.04	0.00	0.03
MgO	0.02	0.03	b.d.	b.d.	b.d.	0.02	b.d.	0.00	0.02	0.00	0.01	0.05	b.d.	b.d.	b.d.	b.d.
CaO	10.96	8.10	7.69	8.42	7.86	8.40	8.17	8.29	7.28	10.41	7.90	6.52	7.96	0.22	0.03	0.02
Na_2O	5.30	6.52	6.67	6.64	6.47	6.42	6.61	7.16	7.52	5.68	6.59	7.68	6.64	0.39	1.70	1.34
K_2O	0.19	0.38	0.43	0.38	0.40	0.36	0.35	0.37	0.36	0.23	0.30	0.62	0.33	14.91	14.38	14.77
SrO	b.d.	0.04	b.d.	b.d.	b.d.	0.01	0.03	b.d.	b.d.	0.04	0.01	b.d.	b.d.	b.d.	b.d.	0.02
Total	98.53	98.15	96.70	97.83	101.09	100.43	97.38	99.71	98.92	100.30	101.47	99.95	99.71	98.53	97.83	97.38
An/%	52.74	39.80	37.92	40.34	39.21	41.10	39.75	38.22	34.16	49.65	39.16	30.80	39.06	1.16	0.15	0.08
Ab	46.18	57.97	59.54	57.50	58.44	56.82	58.23	59.75	63.81	49.06	59.08	65.72	59.00	3.76	15.23	12.12
Or	1.08	2.22	2.54	2.16	2.35	2.08	2.02	2.03	2.03	1.29	1.76	3.49	1.94	95.08	84.62	87.80
*$KD_{(An-Ab)}^{pl-liq}$	0.07	0.12	0.13	0.12	0.13	0.12	0.12	0.13	0.16	0.08	0.13	0.18	0.13			
T/℃		838	830	840	836	843	839	833			838		837			
H_2O/wt.%		4.44	4.61	4.40	4.49	4.34	4.43	4.54			4.44		4.47			

b.d.: below detection limit.
* : after Putirka (2008).

4.2. Zircon U-Pb geochronology

The Sanxianba granite has euhedral prismatic zircons (Fig. 4a). We have examined CL images of more than 200 zircons and found no inherited cores which show rounding and other resorption features (Corfu et al., 2003; Miller et al., 2003; Watson, 1996). Under CL, the inner of zircons (Zrn-earlier) is relatively bright and show distinct oscillatory zone, while the outer (Zrn-later) is relatively black without obvious oscillatory zone (Fig. 4a). Fourteen Zrn-earlier and two Zrn-later with no inclusions were selected to analyze U-Pb isotopes, and the results are listed in Appendix Table A. All the age data are identical within analytical error and yield a weighted mean $^{238}U/^{206}Pb$ age of 226.1 ± 1.8 Ma (Fig. 4b).

4.3. Whole rock geochemistry

Whole rock geochemistry results are listed in Table 1. The calculated CIA values (chemical index of alteration: molar ratios of [Al_2O_3/ (Al_2O_3 + CaO + Na_2O + K_2O] *100) are 52.37–52.54 (Table 1), within the common range of fresh granite (Nesbitt and Young, 1982). It belongs to high-K calc-alkaline series and strong peraluminous granite with ASI value of 1.10–1.11 (Fig. 5a). The normalized Qz-Ab-Or composition of the Sanxianba granite suggests that the magma pressure is near 300 Mpa (Fig. 5b, after Blundy and Cashman, 2001). It has right-dipped REE_N patterns, with medium Eu negative anomalies (Eu/Eu*=0.51–0.54) (Fig. 5c), and relatively high Th, U, but low Ba, Sr and Ti contents (Fig. 5d), similar with the W-bearing granites from the Jiangnan Orogen (Huang and Jiang, 2014; Mao et al., 2017; Wang et al., 2007b). Fluorine content is 1030–1070 ppm, and Cl is 48.6–58.2 ppm. Calculated Zr-saturation temperature (T_{Zr}, Watson and Harrison, 1983) is 809–791 ℃.

4.4. Whole rock Sr and Nd isotopes and zircon Lu-Hf isotopes

The Sanxianba granite has relatively radioactive Sr isotope composition, with initial $^{87}Sr/^{86}Sr$ ratios of 0.71836–0.71906 (Table 1). It also has relatively enriched Nd isotope compositions, with εNd(226 Ma) of −8.58 - −8.85 (Fig. 6a) and Nd model age (T_{DM2}) of 1.70–1.72 Ga.

The Lu-Hf isotope compositions of zircon are listed in Appendix Table B. Zircon from the Sanxianba granite has relatively enriched Hf isotopes, with εHf(t) of −5.12 - −7.05, and Hf model ages of 1.6–1.7 Ga (Fig. 6b).

4.5. In-situ composition of mineral

4.5.1. Feldspar

The EMPA results for feldspar are listed in Table 2. Plagioclase phenocrysts are mainly andesine (An = 30.80–41.10), and sometimes have the labradorite in the core (An = 49.65–52.74) (Fig. 7a). They have normal-zoned texture, with decreasing CaO and increasing Na_2O rim-ward (Fig. 7b). K-feldspar phenocrysts have low contents of CaO (0.02–0.22 wt%) and Na_2O (0.39–1.70 wt%), with Or fraction of 84.62–95.08 (Fig. 7a). Temperature and water contents of magma when plagioclase crystallizes are calculated via methods of Putirka (2005) and Waters and Lange (2015), respectively (Table 2). Whole rock composition is viewed as the melt composition when calculation, and the early plagioclase (An = 41.1–37.9) gives the temperature of 830–843 ℃ and water content of 4.40–4.61 wt%. The labradorite core and rim plagioclase (An < 36) are out the equilibrium with melt (after the method of Putirka, 2008) (Table 2) and thus don't give meaningful results.

4.5.2. Biotite

The *in-situ* compositions of biotite are listed in Table 3. The biotite has 2.04–2.36 wt% TiO_2, 18.43–20.43 wt% FeO, 0.18–0.27 wt% MnO, and 10.66–11.46 wt% MgO, belonging to magnesia biotite (Fig. 7c). Al_2O_3 in biotite is relatively high (Al > 2.80 apfu in formula unit), and plotted in the compositional range of biotite from peraluminous granite (Fig. 7d). It contains relatively high F content from 1.14 to 1.54 wt% and low Cl content from 0.076 to 0.095 wt%. The intercept values of IV(F), IV(Cl), and IV(F/Cl) of biotite is calculated after Munoz (1984) to obtain the relative degree of halogen enrichment in biotite (Table 3). The biotite has low IV(F) and thus is relatively enriched in fluorine, which is comparable to IV(F) of biotite from the scheelite-bearing granite (Fig. 7e). Calculated water content in the biotite after Tindle and Webb (1990) is 3.30–3.42 wt% (Fig. 7f). Biotite has 579–833 ppm Rb, 1837–4454 ppm Ba, 34.9–50.8 ppm Nb, and 1.08–2.18 ppm Ta, with Rb/Ba ratios 0.15–0.45 and Nb/Ta ratios 23.26–32.31 (Fig. 7g). It also has 14.4–17.9 ppm Sn, and 1.12–3.37 ppm W (Fig. 7h).

4.5.3. Apatite

Apatite from the Sanxianba granite has relatively high contents of FeO, MnO, F, but low Cl, similar with those from the tungsten-bearing granite (Table 4, Fig. 8a-b). FeO (0.400–0.913 wt%) and FeO/MnO ratios (0.98–4.06) of the Ap-earlier are relatively high, while those of the Ap-later lower (0.15–0.359 wt% and 0.410–1.04, respectively) (Fig. 8). Their MnO contents are comparable (Fig. 8a). The Ap-earlier has

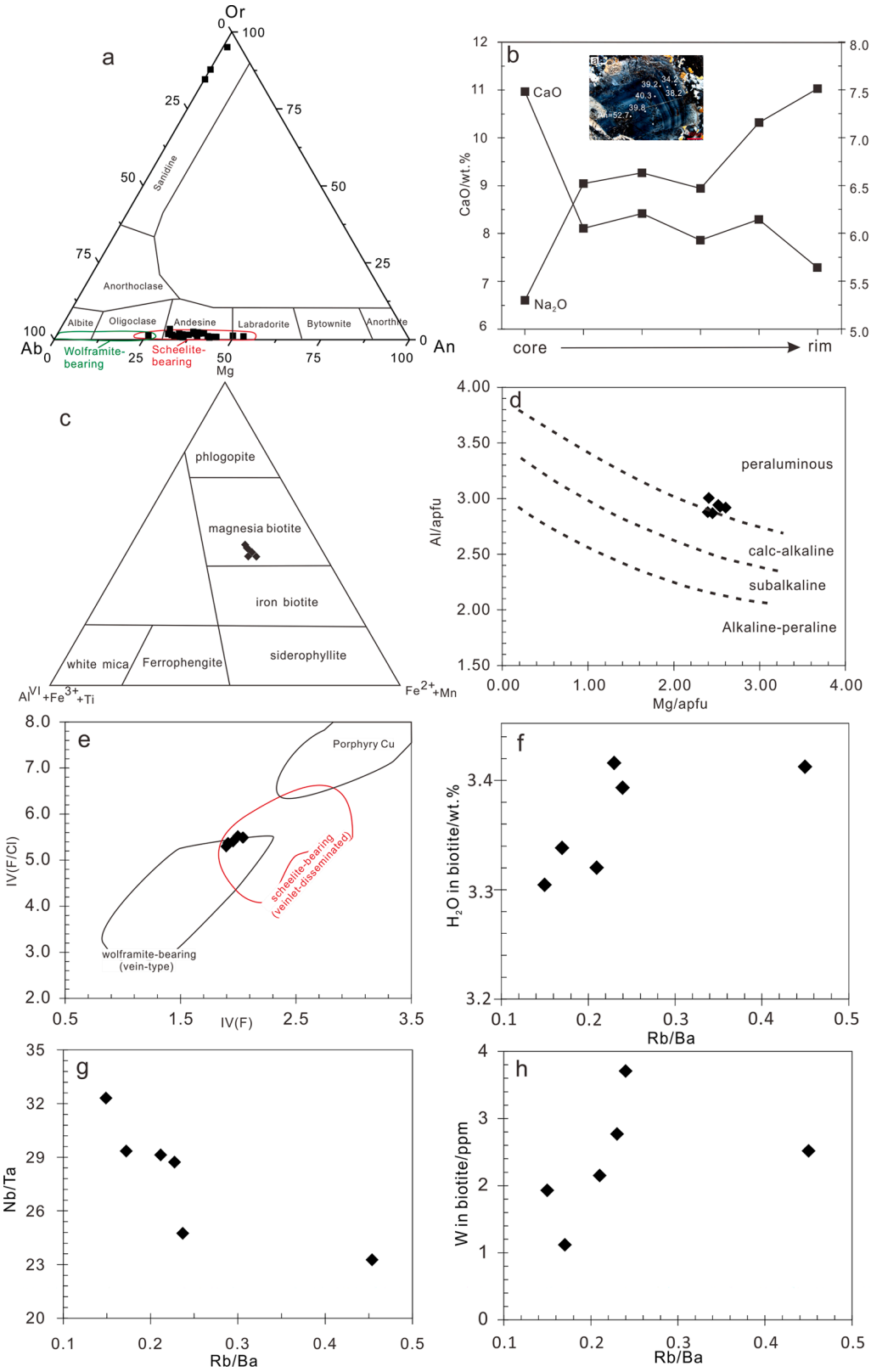

Fig. 7. The *in-situ* mineral compositions of feldspar (a-b) and biotite (c-h) in the Sanxianba granite. **a:** An-Ab-Or triangle diagram of feldspar. The plagioclase compositions of both the wolframite-bearing granite and scheelite-bearing granite are according to Zhang et al. (2017), and Mao et al. (2017) and Xie et al. (2018b), respectively. **b:** Compositional profiles of Na_2O and K_2O in a normal-zoned plagioclase phenocryst. **c:** Classification of biotite (after Foster, 1960). **d:** Al–Mg diagram for biotite (after Stussi and Cuney, 1996). **e:** Intercept value IV(F/Cl) plots against IV(F) for biotite. The biotite compositions for porphyry Cu, scheelite-bearing granite and wolframite-bearing granite are from Munoz (1984), Mao et al. (2017) and Zhang et al. (2016), and Jiang et al. (2005) and Li et al. (2013), respectively. **f:** H_2O vs. Rb/Ba, **g:** Nb/Ta vs. Rb/Ba, and **h:** W vs. Rb/Ba in biotite.

Table 3
EMP (in wt. %) and LA-ICP-MS (in ppm) compositions of the biotite from the Sanxianba granite.

sample	ZK007-29				ZK006-33	
analyse No.	01	02	03	04	06	07
(wt. %)						
SiO_2	36.41	36.44	35.25	36.39	36.78	36.92
TiO_2	2.29	2.27	2.04	2.36	2.14	2.24
Al_2O_3	16.58	16.19	16.57	16.58	16.75	16.24
FeO	20.03	20.43	20.34	19.27	18.96	18.43
MnO	0.27	0.25	0.26	0.27	0.27	0.27
MgO	11.2	10.66	10.5	11.38	11.34	11.46
CaO	0.01	bd.	0.02	0.00	0.06	0.03
Na_2O	0.22	0.25	0.22	0.33	0.32	0.27
K_2O	9.56	9.05	9.44	9.35	9.28	9.29
F	1.22	1.15	1.14	1.44	1.28	1.54
Cl	0.09	0.08	0.09	0.08	0.1	0.08
H_2O*	3.42	3.41	3.34	3.30	3.39	3.32
O = F,Cl	0.50	0.62	0.54	0.50	0.56	0.67
Total	101.30	100.18	99.21	100.75	100.67	100.09
(ppm)						
Li	566	661	642	634	662	665
Sc	64.8	65.2	59.1	62.3	67.4	63.2
V	506	420	566	441	433	419
Cr	345	250	284	347	316	299
Co	39.6	49.3	36.8	40.1	26.5	44.3
Ga	50.8	50.5	47.3	52.1	59	51.7
Rb	791	833	579	663	756	696
Sr	0.35	0.21	0.5	0.25	0.32	0.22
Nb	42	50.8	38.8	34.9	53.1	42
Sn	16.6	14.4	15.5	16.8	15.5	17.9
Cs	33	34.1	20.2	43.3	29.4	37.9
Ba	3478	1837	3367	4454	3193	3289
Ta	1.46	2.18	1.32	1.08	2.15	1.44
W	2.77	2.52	1.12	1.93	3.71	2.15
Nb/Ta	28.73	23.26	29.35	32.31	24.74	29.13
Rb/Ba	0.23	0.45	0.17	0.15	0.24	0.21

b.d.: below detection limit.
* afterTindle and Webb (1990).

3.035–3.578 wt% F, 0.01–0.05 wt% Cl, 0.06–0.15 wt% Na_2O, and no>0.13 wt% La_2O_3 (Fig. 8c-f). Fluorine content in the Ap-later is up to 4.05 wt%, but Cl, Na_2O and La_2O_3 contents are<0.05 wt%, 0.15 wt% and 0.07 wt%, respectively (Fig. 8c-f).

4.5.4. Zircon

In-situ LA-ICP-MS compositions of zircon are listed in Appendix Table C. All the zircons have left-dipped REE_N patterns with negative Eu-anomaly and positive Ce-anomaly (Fig. 9a). From Zrn-earlier to Zrn-later, P and REE + Y increase (Fig. 9b), while the Eu/Eu* and $(Sm/Yb)_N$ ratios decrease (Fig. 9c). Thorium, U, Nb and Ta contents gradually increase in the zircons with fractionation, but Th/U ratios decrease (Fig. 9d-e; Appendix Table C). The Nb/Ta ratios of the zircons decrease in the Zrn-earlier, and have a faint increase in the Zrn-later (Fig. 9e). The tungsten contents in the Zrn-earlier (<0.05 ppm) are mostly below the detection limit, while the Zrn-later has relatively high contents of W (0.03–2.81 ppm) (Fig. 9f). The calculated crystallization temperature of the zircons ($T_{Zrn\text{-}Ti}$) after Ferry and Watson (2007) are from 808℃ to 527 ℃ (Fig. 10). The calculated oxygen fugacity using zircon oxybarometer of Loucks et al. (2020) is below FMQ buffer (Fig. 10).

5. Discussion

5.1. Petrogenesis of the Sanxianba granite

The Sanxianba granite is strongly peraluminous, and has relatively high contents of Si and Rb, but low Ba, Sr and Ti (Fig. 5), similar to the typical compositions of S-type granite (Champion and Bultitude, 2013; Chappell and White, 1992, 2001; Clemens, 2003; Wu et al., 2003; 2017) and the W-bearing granite from the Jiangnan Orogen (Fig. 5; Huang and Jiang, 2014; Mao et al., 2017; Wang et al., 2007b). It also has the typical crust-derived Sr-Nd-Hf isotope compositions (Table1, Fig. 6). The apatite and zircon have compositions similar to those from S-type granites (Burnham and Berry, 2017; Sha and Chappell, 1999; Fig. 8a-b, 9b) and W-Sn-bearing granites (Fig. 8a-b; Ding et al., 2015; Rasmussen and Mortensen, 2013).

Assessing temperatures of magma that solidified to form plutonic rock can provide important enlightment for its petrogenesis (Chappell et al., 2004; Miller et al., 2003). The zircon saturation temperature (T_{Zr}, Watson and Harrison, 1983) can serve as the minimum estimates of temperature if the magma is lacking inherited zircon (Miller et al., 2003). The Sanxianba granite is inheritance-poor and thus the T_{Zr} indicates the temperature of the Sanxianba magma is no less than the 809 ℃ (Table 1). This result is consistent with the calculated crystallization temperature of the early plagioclase (up to 843 ℃; Table 2) and $T_{Zrn\text{-}Ti}$ (up to 808 ℃; Fig. 10). Thus the Sanxianba granite belongs to "hot granites" of Miller et al. (2003), and might have originated from biotite dehydration melting in the crust. The relatively high CaO/Na_2O ratios (0.65–0.66) and low Al_2O_3/TiO_2 ratios (41.6–44.4) of the Sanxianba granite suggest it may be derived from high-temperature partial melting of the biotite-rich psammitic rocks (Patiño Douce and Johnston, 1991; Patiño Douce and Beard, 1995; Skjerlie and Johnston, 1996; Sylvester, 1998 and references therein). The whole rock Nd isotope data indicates it may originate from the Neoproterozoic Banxi group strata (Fig. 6a). The Banxi Group is a series of tuffaceous-bearing clastic sediments, in which metasandstone is relatively rich in CaO and TiO_2 with average ~ 88 ppm Rb (Gu et al., 2003) and 8.2 ppm W (Yang, 1992). The Sanxianba stock emplaced at ~226 Ma (Fig. 4). The contemporaneous mafic rocks are also found in the district (c.f. Dai et al., 2008; Jin et al., 2017). Thus mafic magma underplating might have taken place during this period in the South China (Wang et al., 2007b; Zhao et al., 2017b), and provided heat for the high-temperature partial melting of the Banxi Group metasandstone to generate the Sanxianba magma.

Here we select the Banxi Group metasandstone as the source rock and use the partial melting model of Shaw (1970) to model the origin of the Sanxianba magma. Biotite-dehydration melting (biotite + feldspar + aluminous silicate + quartz = melt + garnet, Nabelek and Bartlett, 2001) is selected as the melting reaction. Rubidium mainly partitions into mica and feldspar, rather than accessory minerals (c.f. Blundy and Wood, 1991) and thus is used here to model melting process. The modal abundance of minerals in source rock (see Appendix Table D) is calculated through mass balance using the whole rock composition (after Li et al., 2020). The Rb content of the primary magma of the Sanxianba (164 ppm) is calculated through the Rb content of the earliest biotite (579 ppm) enveloped in plagioclase (see Appendix Table D for more details). The modeling shows that ~35% partial melting of the Banxi Group metasandstone can produce primary magma of the Sanxianba granite (Appendix Table D Fig. 11a) and that its tungsten content is ~21 ppm, comparable to the tungsten contents in the W-bearing granites in South China (Fig. 11b; Huang and Jiang, 2014; Mao et al., 2017; Wang et al., 2007b; Zhang et al., 2017; See the Appendix Table D for more details). Similar partial melting modeling was conducted by Simons et al. (2016) and their results also indicated that ~ 30% biotite-dehydration melting of the metagreywacke can produce the W-Sn-bearing granite in the Cornubian Batholith.

5.2. Tungsten enrichment during magma evolution

Major mineral phases may be important carriers of specific trace elements (e.g. Sr and Eu in plagioclase and Rb in biotite), however the budget of most other trace elements (e.g. REE, Th and U) in silicic magmas is controlled by crystallization of accessory minerals such as apatite and zircon due to their high and distinct partition coefficients (c.f. Bachmann et al., 2005; Rubatto and Hermann, 2007). Relatively protracted timescales of zircon, combined with its compositions, gives it a potential proxy to record the evolution of an ore-forming magma

Table 4
EMP compositions (in wt. %) of the apatite from the Sanxianba granite.

Type	Ap-earlier (inclusions in biotite)										
sampl	ZK006-34							ZK006-35			
spot	1	2	3	4	5	6	7	16	17	18	19
P_2O_5	40.04	41.26	40.50	39.84	40.72	40.35	40.42	40.01	41.96	41.38	42.04
SiO_2	b.d.	b.d.	0.05	0.25	0.24	0.27	0.17	0.18	b.d.	b.d.	b.d.
TiO_2	b.d.	0.02	0.04	0.07	0.03	0.05	0.02	0.01	b.d.	0.01	0.04
Al_2O_3	b.d.	0.03	b.d.	b.d.	b.d.	b.d.	b.d.	b.d.	b.d.	0.01	0.02
FeO	0.91	0.51	0.59	0.84	0.68	0.65	0.59	0.46	0.40	0.43	0.47
MnO	0.49	0.48	0.27	0.22	0.20	0.16	0.35	0.22	0.41	0.13	0.25
CaO	53.55	55.34	54.26	53.65	53.94	53.95	53.92	53.95	54.64	53.96	54.32
Na_2O	0.09	0.13	0.13	0.10	0.07	0.06	0.12	0.12	0.15	0.12	0.12
Ce_2O_3	0.21	0.28	0.15	0.13	0.31	0.19	0.25	0.13	0.07	0.12	0.11
La_2O_3	0.11	0.13	0.05	0.07	b.d.	0.03	0.13	0.03	0.06	0.05	b.d.
F	3.04	3.58	3.23	3.27	3.16	3.10	3.22	3.34	3.41	3.24	3.36
Cl	0.05	0.04	0.04	0.01	0.03	0.03	0.03	0.04	0.04	0.02	0.04
O = F,Cl	1.29	1.52	1.37	1.38	1.34	1.31	1.36	1.42	1.45	1.37	1.42
Total	97.14	99.93	97.94	97.04	97.97	97.56	97.68	97.04	99.72	98.14	99.41
FeO/MnO	1.87	1.07	2.19	3.82	3.40	4.06	1.69	2.09	0.98	3.31	1.88

occurrence	Ap-later (isolated grain in the matrix)							
sample	ZK007-29			ZK006-35				
spot	8	9	10	11	12	13	14	15
P_2O_5	40.36	41.28	40.89	41.96	41.57	41.77	42.59	41.75
SiO_2	b.d.	0.05	0.00	b.d.	b.d.	b.d.	b.d.	b.d.
TiO_2	b.d.	b.d.	b.d.	0.00	b.d.	b.d.	0.00	0.01
Al_2O_3	b.d.	b.d.	b.d.	0.01	b.d.	0.01	0.00	0.02
FeO	0.26	0.31	0.28	0.23	0.17	0.27	0.15	0.36
MnO	0.25	0.32	0.32	0.38	0.40	0.38	0.37	0.45
CaO	56.06	55.29	54.16	55.58	54.95	55.41	55.67	55.58
Na_2O	0.08	0.10	0.07	0.09	0.11	0.14	0.15	0.09
Ce_2O_3	0.11	0.16	0.11	0.12	0.27	0.19	0.13	0.19
La_2O_3	0.05	0.03	b.d.	b.d.	0.02	0.07	0.01	0.07
F	3.17	3.68	3.37	3.20	3.71	3.67	3.86	4.05
Cl	0.02	0.02	0.06	0.03	0.04	0.04	0.04	0.05
O=F,Cl	1.34	1.55	1.43	1.35	1.57	1.55	1.63	1.72
Total	99.10	99.51	97.85	100.39	99.37	100.17	101.19	100.64
FeO/MnO	1.04	0.97	0.88	0.62	0.43	0.71	0.41	0.80

b.d. : below detection limit.

chamber from zircon saturation through to emplacement and solidification (Large et al., 2018).

REE can enter the zircon lattice through substituting for Zr (Hoskin and Schaltegger, 2003). Controlled by the proximity of their radii and valence state to zirconium's, the REE in igneous zircon is characterized by a steeply-rising normalized pattern from the LREE to the HREE with a positive Ce-anomaly and negative Eu-anomaly (Hoskin and Schaltegger, 2003; Loader et al., 2017). Both Zrn-earlier and Zrn-later from the Sanxianba granite have characteristic REE patterns of magmatic zircon (Fig. 9a), indicating a magmatic-origin. The nearly 1:1 relation between concentrations of P and REE + Y in them (Fig. 9b) indicates the dominant "xenotime" substitution mechanism ($(Y, REE)^{3+} + P^{5+} = Zr^{4+} + Si^{4+}$, Hoskin and Schaltegger, 2003) for REE. During the evolution of the Sanxianba magma, zircons record a decreasing crystallization temperature and the relatively constant oxygen fugacity (Fig. 10), indicating progressive cooling and crystallization of a magma reservoir that remained unaffected by any chemical or thermal rejuvenation (c.f. Large et al., 2018). The normal compositional zones of the plagioclase phenocrysts also show progressive cooling (Winter, 2012, Fig. 7b).

Europium anomalies in the zircons can be influenced by the redox conditions (c.f. Loader et al., 2017; Trail et al., 2012) and/or by co-crystallization of Eu-bearing mineral phases like plagioclase (c.f. Deering et al., 2016) and titanite (Loader et al., 2017). The oxygen fugacity of the Sanxianba magma is relatively constant (Fig. 10), hence it does not lead to the decreasing Eu/Eu* ratios in zircons. Magmatic titanite is not found in the Sanxianba granite. Thus, the negative Eu-anomaly variation in zircons probably reflects the co-crystallization of plagioclase. The $(Sm/Yb)_N$ ratios in zircons also decrease with the fractionation (Fig. 9c), indicating the co-crystallization of apatite which preferentially incorporates Sm over Yb (Deering et al., 2016). With the Sanxianba magma fractionation, Th and U will gradually increase. This process is recorded by the zircon (Fig. 9d). The Zrn-later has elevated Th and U contents (Fig. 9d), indicating a relatively fractionated later melt. The decreasing Th/U ratios in zircons with fractionation (Fig. 9d) reflect the greater incompatibility of U than Th in crystallizing mineral assemblage.

Tantalum and niobium are incompatible lithophile elements and normally show an increase accompanied by a decrease of the Nb/Ta ratio during the magma fractionation (c.f. Dostal and Chatterjee, 2000; Stepanov et al., 2014). The enrichment trend of Nb and Ta in the Sanxianba magma with fractionation is recorded by the increasing Nb and Ta contents in the zircons (Appendix Table C, Fig. 9e). The decreasing Nb/Ta ratios in the Zrn-earlier (Fig. 9e) may reflect the co-crystallization of biotite which preferentially incorporates Nb over Ta (Stepanov et al., 2014). While the faint increase of Nb/Ta ratios in the Zrn-later (Fig. 9e) cannot be explained by the continuous crystallization. One possible explanation is that there is Cl-rich fluid exosolution. The Cl-rich fluid will preferentially sequester Ta over Nb (Keppler, 1996) and thus the residual melt will have increased Nb/Ta ratios. Both Nb and Ta are generally not likely to partition into fluid ($D^{fluid/melt} < 1$, Keppler, 1996), and hence fluid exosolution will not interrupt their enrichment trend in the fractionated melt.

Experiments show that tungsten solubility in granitic melt is more than 1000 ppm WO_3 (Štemprok, 1990), and can be up to 2.68 wt% in fluxing-rich evolved melts (Che et al., 2013). Tungsten is incompatible in most rock-forming minerals and thus will concentrate in evolved melt during differentiation (Černý et al., 2005; Linnen and Cuney, 2005). The

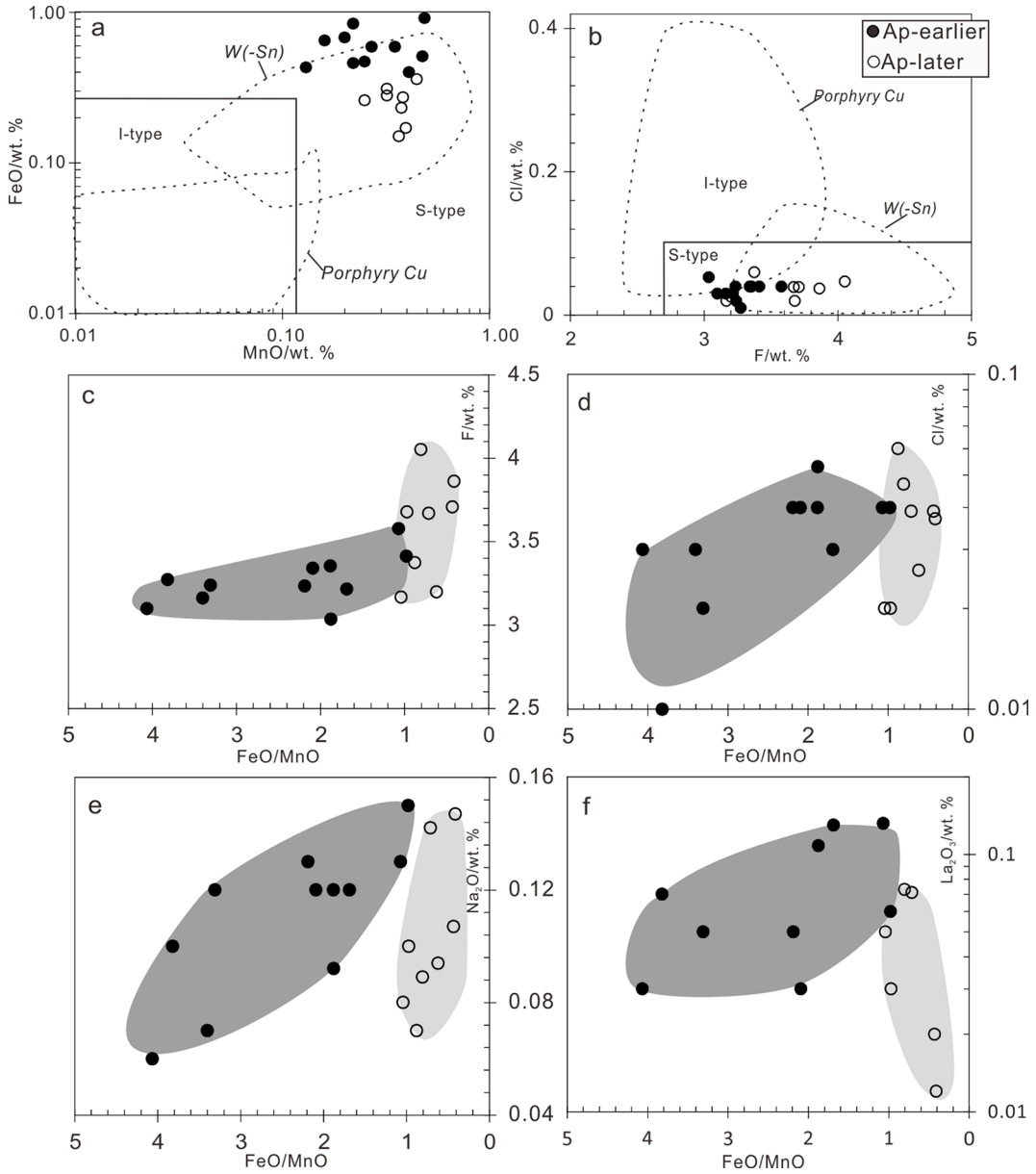

Fig. 8. Compositions of the apatite in the Sanxianba granite. **a**: MnO vs. FeO; **b:** F vs. Cl; **c:** FeO/MnO vs. F; **d:** FeO/MnO vs. Cl; **e:** FeO/MnO vs. Na_2O; **f:** FeO/MnO vs. La_2O_3. Data sources in **a** and **b**: the compositional ranges of apatite from the S- and I-type granite (Sha and Chappell, 1999), the porphyry Cu deposit (Pan et al., 2016), and the W(-Sn) deposit (Ding et al., 2015; Rasmussen and Mortensen, 2013).

tungsten contents in the zircons show an enrichment trend with crystallization fractionation (Fig. 9f), and the similar trend is also recorded by the phenocryst biotite (Fig. 7h). This suggests a gradual enrichment of tungsten in the magma with fractionation. Although the partition coefficient of tungsten between zircon and melt is not available, the experimental studies show that the partition coefficient of tungsten between minerals and basaltic melts has limited variation with different temperature and pressure (Adam and Green, 2006). Hence, it is speculated that the partition coefficient of tungsten between zircon and melts might have also been nearly constant. Thus, the variation of W in the melt can be estimated based on the concentration of W in the zircon. If so, increase of W in zircon from early 0.05 ppm to later 2.81 ppm (Fig. 9f) implies that the tungsten contents in the evolved melt can increase by about fifty times.

5.3. *Fluxing components (H_2O, F, Cl, P) in the Sanxianba magma*

The water content of granitic magma can be deduced from the crystallization sequence of hydrous minerals. Experiments show that in the H_2O-poor melt (e.g <1.5 wt%) biotite is a late-saturated mineral facies after both the K-feldspar and quartz (Maaløe and Wyllie, 1975), whereas in the H_2O-rich melt (>4 wt%) biotite is a precursor earlier than plagioclase (Naney, 1983). Some of the biotites in the Sanxianba granite occur as mineral inclusions wrapped in plagioclase (Fig. 3d), suggesting an early-saturated biotite mineral phase in the magma. Thus, the water contents in the early Sanxianba magma will be no less than 4 wt%. This inference is consistent with the calculated water contents using the plagioclase hygrometer (~4.4 wt%, Table 2). The water enrichment trend in the magma with fractionation is recorded by the water contents in biotite (Fig. 7f).

The Sanxianba granite has high F contents (1030–1070 ppm) and low Cl contents (48.6–58.2 ppm), which suggest it may be relatively F-

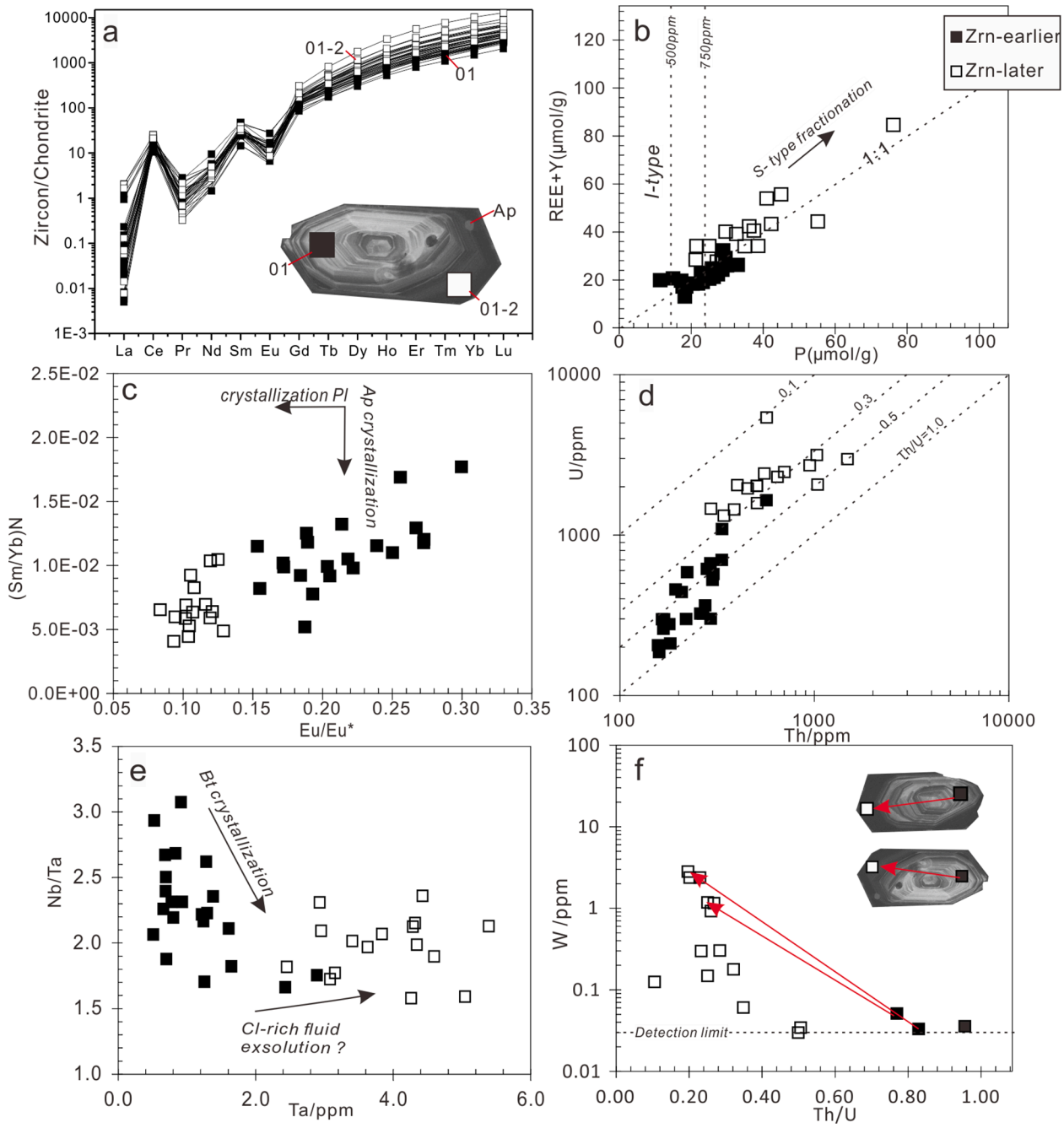

Fig. 9. Textures and *in-situ* REE and trace elements of zircons from the Sanxianba granite. **a:** Chondrite-normalized REE patterns, inset shows the representative texture of zircon under CL, and squares on it are analyzed spots. **b:** Molar concentrations of REE + Y vs. P in zircon. **c:** Eu/Eu* vs. $(Sm/Yb)_N$; **d:** Th vs. U; **e:** Ta vs. Nb/Ta; **f:** Th/U vs. W. Chondrite values are from Sun and McDonough (1989). The I- and S-type granite trend/range in (b) is according to Burnham and Berry (2017).

rich but Cl-poor. This is consistent with the halogen compositions of both the biotite and apatite in the Sanxianba granite (Figs. 7, 8). In the muscovite- and fluorite-free granitoids, most (70 to 90%) of the F is contained in biotite, with the remainder being in apatite, and biotite is also the main sink of Cl (Grabezkev et al., 1979; Teiber et al., 2014). Chloritization of biotite may release significant amounts of F and Cl (Teiber et al. 2014) and cause the whole rock halogen content lower than its true value. Biotite suffered from a different degree of chloritization in the Sanxianba granite (Fig. 3c), thus the whole rock F and Cl content in the granite may be a minimum estimate of actual content.

It has been experimentally confirmed that F and Cl are compatible in apatite (c.f. Doherty et al., 2014; Mathez and Webster, 2005). Thus, the actual budget of F and Cl in the magma can be recorded by the halogen concentrations of apatite. The Ap-earlier records a process of Cl enrichment (Fig. 8d) during the magma evolution. Chlorine can complex with Na and LREE in the melt (Webster, 1992, 1997), thus the elevated Cl contents in melt will facilitate the enrichment of Na and LREE (Webster and Rebbert, 2001), just as recorded by the Ap-earlier (Fig. 8e-f). In the Ap-later, the Cl enrichment is terminated (Fig. 8d), suggesting the Cl content in the later melt decreases. There may be fluid exsolution during the later period of magma evolution. The exsolved fluid sequesters the Cl from the melt ($D_{Cl}^{fluid/melt} > 1$, Villemant and Boudon, 1999) to lead to Cl decrease in the melts. The exsolved Cl-rich fluids may also sequester the Cl-complexed elements from the melt, like Na (Audétat et al., 2000) and LREE (Migdisov et al., 2016; Tsay et al., 2014). This can explain why the Na_2O and LREE (La_2O_3) contents in the

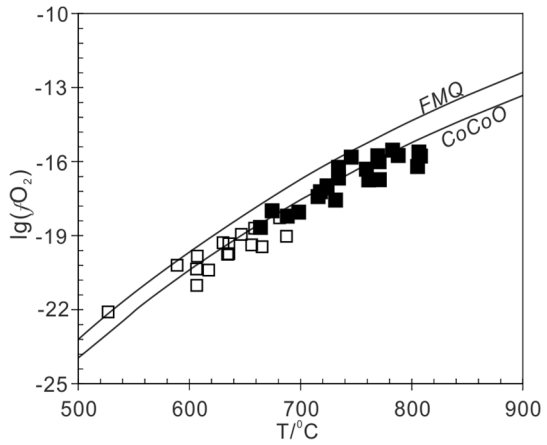

Fig. 10. Calculated temperature (after Ferry and Watson, 2007) and oxygen fugacity (after Loucks et al., 2020) of the Sanxianba magma using the zircon compositions. Quartz-fayalite-magnetite (FMQ) and CoO-Co-O_2 (CoCoO) buffers shown are from Frost (1991).

Ap-later decrease (Fig. 8e-f).

Fluorine and P are more compatible in the melt than in fluid ($D_F^{fluid/melt} < 1$, Villemant and Boudon, 1999), and hence further concentrated in the evolved melt, just as recorded by both the Ap-later (Fig. 8c) and Zrn-later (Fig. 9b). High F and P contents in the melt can increase the H_2O solubility in the melt (Audétat et al., 2000; Holtz et al., 1993). Thus water, F and P will increase in the evolved melt until they reach oversaturation to generate ore-forming fluids.

5.4. Tungsten mineralization in the Muguayuan deposit

Fluxing components like H_2O, F and P are essential for the formation of magmatic-hydrothermal ore deposits as they can greatly influence the crystallization fractionation, ore elements enrichment, subsequent fluid exsolution and ore elements transport in the fluid, all of which are important processes in ore formation (Audétat and Simon, 2012; Candela, 1997; Candela and Piccoli, 2005; Hedenquist and Lowenstern, 1994; Williams-Jones and Migdisov, 2014). Fluorine, P and H_2O enrichment is a common scenario in the W-Sn rare metal granites and can promote the differentiation of magma (c.f. Bea et al., 1992; Che et al., 2013; Linnen and Cuney, 2005; Webster et al., 1998). High H_2O, F and P in the melt can effectively increase the amount of non-bridging oxygen through depolymerizing the melt structure, and thus enhance the compatibility of tungsten and other rare metal elements in melts (Candela, 1992; Dostal and Chatterjee, 2000; Keppler, 1993; Rickers et al., 2006; Timofeev and Williams-Jones, 2015; Timofeev et al., 2017; Webster et al., 1998). In the Sanxianba granite, F, P and H_2O are continuously enriched in the evolved melt during the magma fractionation. The elevated fluxing components in the evolved melt may lower the solidus temperature of hydrous granitic systems (Fig. 10) and prolong the magma fractionation time to promote further enrichment of tungsten in the evolved melt.

Magma related to ore deposits usually has relatively high contents of water (>4 wt%; Sillitoe, 2010). However, Chiaradia (2020) proved that oversaturation of H_2O would lead to the Cl-rich exsolution of fluid at early fractionation stage. The Sanxianba granite originates from the ~35% partial melting of the Banxi Group metasandstone, with ~21 ppm tungsten in the primary melt (see modeling in Appendix Table D, Fig. 11). The water content in the early Sanxianba magma is ~4.4 wt%, within the range of common fertile magma for ore deposit (4–6 wt%, Chiaradia, 2020; Sillitoe, 2010). When H_2O starts to be saturated with the magma fractionation in the deep magma chamber, Cl-rich and W-poor fluids will exsolve from the melt (c.f. Audétat et al., 2000), resulting in the early albitization and chloritization of feldspar and biotite phenocryst, respectively.

During the shallow-ward emplacement, their solubility in the melt will decrease due to decompression (Audétat et al., 2000; Lowenstern, 1994; Sparks et al., 1994), triggering the exsolution of F-, P-, and W-rich fluids. Following emplacement, the apex of the intrusion cools and crystallizes first, forming a solidified shell (c.f. Burnham, 1985, 1997; Kirwin, 2005). The exsolved fluids from the underlying magma continuously supply upward, react with the early-formed shell along fractures and then result in greisenization and phyllic alteration. During these alteration, decomposition of calcium-rich plagioclase (Fig. 7a) releases calcium (Ca^{2+}) into fluids (Hemley and Jones, 1964; Jiang et al., 2015; Li et al., 2018; Zhang et al., 2018). Calcium combines with tungsten in the fluids to precipitate scheelite in those fractures during the evolution of fluids, leading to veinlet-disseminated scheelite mineralization (Li et al., 2018).

6. Conclusions

1. The Sanxianba granite shows affinity to S-type, which is derived from a W-rich melt originated by high-temperature partial melting of the Banxi Group metasandstone.
2. During the magma evolution, W, F, P, H_2O and other incompatible elements are gradually concentrated and form a W-rich evolved melt.
3. The exsolved fluids from the W-rich evolved melt react with granite, forming greisenization and phyllic alteration, and veinlet-disseminated scheelite mineralization.

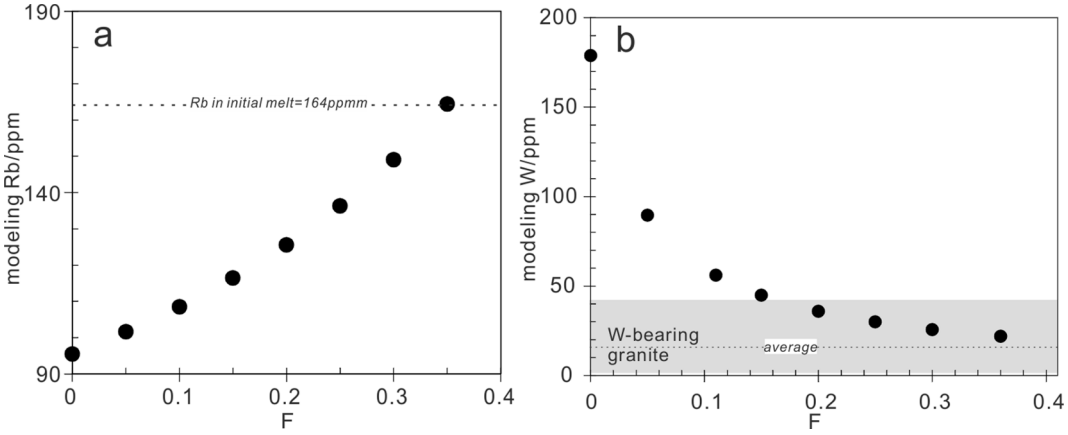

Fig. 11. The trace element modeling results of the Banxi Group metasandstone. **a:** Rubidium content in modeling melt. **b:** Tungsten content in modeling melt. The range of tungsten contents in the W-bearing granites is according to Huang and Jiang (2014), Mao et al. (2017), Wang et al. (2007b) and Zhang et al. (2017).

Declaration of Competing Interest

The authors declare that they have no known competing financial interests or personal relationships that could have appeared to influence the work reported in this paper.

Acknowledgements

This work is funded by the National Natural Science Foundation of China (grant NO. 41830428) and the National Science Fund for Distinguished Young Scholars (42025301). We are grateful to Eimear Deady, Yanbo Chen, and one anonymous reviewer for their very insightful, helpful and constructive comments that greatly improved this manuscript. We sincerely thank Juan Li from the State Key Laboratory for Mineral Deposits Research at Nanjing University and Liang Li from the FocuMS Laboratory (Nanjing, China) for their technical assistance with SEM and LA–ICP–MS analyses, respectively.

Appendix A. Supplementary data

Supplementary data to this article can be found online at https://doi.org/10.1016/j.oregeorev.2021.104406.

References

Adam, J., Green, T., 2006. Trace element partitioning between mica-and amphibole bearing garnet lherzolite and hydrous basanitic melt: I. Experimental results and the investigation of controls on partitioning behaviour. Contrib. Mineral. Petrol. 152 (1), 1–17.

Audétat, A., Gnther, D., Heinrich, C.A., 2000. Magmatic-hydrothermal evolution in a fractionating granite: a microchemical study of the Sn-W-F-mineralized mole granite (Australia). Geochim. Cosmochim. Acta 64 (19), 3373–3393.

Audétat, A., Simon, A. C., 2012. Magmatic controls on porphyry copper genesis. In: Hedenquist, J. W., Harris, M. and Camus F. (Eds.) Geology and Genesis of Major Copper Deposits and Districts of the world: A Tribute to Richard H. Sillitoe. Econ. Geol. 16, 553–572.

Audétat, A., 2019. The metal content of magmatic-hydrothermal fluids and its relationship to mineralization potential. Econ. Geol. 114 (6), 1033–1056.

Azadbakht, Z., Lentz, D.R., McFarlane, C.R., Whalen, J.B., 2020. Using magmatic biotite chemistry to differentiate barren and mineralized Silurian-Devonian granitoids of New Brunswick, Canada. Contrib. Mineral. Petrol. 175 (7), 1–24.

Bachmann, O., Dungan, M., Bussy, F., 2005. Insights into shallow magmatic processes in large silicic magma bodies: the trace element record in the Fish Canyon magma body, Colorado. Contrib. Mineral. Petrol. 149, 338–349.

Bea, F., Fershtater, G., Corretgé, L.G., 1992. The geochemistry of phosphorus in granite rocks and the effect of aluminium. Lithos 29 (1–2), 43–56.

Berni, G.V., Wagner, T., Fusswinkel, T., Wenzel, T., 2017. Magmatic-hydrothermal evolution of the Kymi topaz granite stock, SE Finland: mineral chemistry evidence for episodic fluid exsolution. Lithos 292, 401–423.

Blundy, J., Cashman, K., 2001. Ascent-driven crystallisation of dacite magmas at Mount St Helens, 1980–1986. Contrib. Mineral. Petrol. 140 (6), 631–650.

Blundy, J.D., Wood, B.J., 1991. Crystal-chemical controls on the partitioning of Sr and Ba between plagioclase, feldspar, silicate melts and hydrothermal solutions. Geochim. Cosmochim. Acta 55, 193–209.

Breiter, K., Frýda, J., Seltmann, R., Thomas, R., 1997. Mineralogical evidence for two magmatic stages in the evolution of an extremely fractionated P-rich rare-metal granite: the Podlesí stock, Krušné hory, Czech Republic. J. Petrol. 38 (12), 1723–1739.

Brugger, J., Lahaye, Y., Costa, S., Lambert, D., Bateman, R., 2000. Inhomogeneous distribution of REE in scheelites and the dynamics of Archaean hydrothermal systems (Mt. Charlotte and Drysdale gold deposits, Western Australia). Contrib. Mineral. Petrol. 139, 251–264.

Brugger, J., Etschmann, B., Pownceby, M., Liu, W., Grundler, P., Brewe, D., 2008. Oxidation state of europium in scheelite: Tracking fluid-rock interaction in gold deposits. Chem. Geol. 257, 26–33.

Burnham, A.D., Berry, A.J., 2017. Formation of Hadean granites by melting of igneous crust. Nat. Geosci. 10 (6), 457–461.

Burnham, C.W., 1985. Energy release in subvolcanic environments; implications for breccia formation. Econ. Geol. 80 (6), 1515–1522.

Burnham, C.W., 1997. Magmas and hydrothermal fluids. In: Barnes, H.L. (Ed.), Geochemistry of hydrothermal deposits, 3rd ed. Wiley, New York, pp. 63–123.

Candela, P.A., 1992. Controls on ore metal ratios in granite-related ore systems: an experimental and computational approach. Trans. Roy. Soc. Edin. Earth Sci. 83 (1–2), 317–326.

Candela, P.A., 1997. A review of shallow, ore-related granites: textures, volatiles, and ore metals. J. Petrol. 38, 1619–1633.

Candela, P. A., Piccoli, P. M., 2005. Magmatic processes in the development of porphyry-type ore systems. In: Hedenquist, J. W., Thompson, J. F. H., Goldfarb, R. J. & Richards, J. P. (Eds.) Econ. Geol. 100th Anniversary Volume: Society of Economic Geologists, Littleton, Colorado, pp. 25–37.

Černý, P., Blevin, P.L., Cuney, M., London, A.D., 2005. Granite-related ore deposits. Econ. Geol. 100th Anniversary Volume, 337–370.

Chappell, B.W., White, A.J.R., 1992. I-and S-type granites in the Lachlan Fold Belt. Trans. Roy. Soc. Edin. Earth Sci. 83, 26.

Chappell, B.W., White, A.J.R., 2001. Two contrasting granite types: 25 years later. Aust. J. Earth Sci. 48, 489–499.

Chappell, B.W., White, A.J.R., Williams, I.S., Wyborn, D., 2004. Low-and high-temperature granites. Trans. Roy. Soc. Edin. Earth Sci. 95, 125–140.

Champion, D.C., Bultitude, R.J., 2013. The Geochemical and Sr-Nd Isotopic Characteristics of Paleozoic fractionated S-types Granites of north Queensland: Implications for S-type Granite Petrogenesis. Lithos 162–163, 37–56.

Che, X.D., Linnen, R.L., Wang, R.C., Aseri, A., Thibault, Y., 2013. Tungsten solubility in evolved granitic melts: An evaluation of magmatic wolframite. Geochim. Cosmochim. Acta 106, 84–98.

Chen, W. D., 2016. A Study on Caledonian and Indosinian Mineralization of Dushiling Tungsten Deposit in the Yuechengling Area, Northern Guangxi, China. Doctoral Dissertations & Master's Theses, Nanjing University.

Chiaradia, M., 2020. How much water in basaltic melts parental to porphyry copper deposits? Front. Earth Sci. 8 (138).

Chu, Y., Lin, W., Faure, M., Wang, Q.C., Ji, W.B., 2012. Phanerozoic tectonothermal events of the Xuefengshan Belt, central South China: implications from U-Pb age and Lu-Hf determinations of granites. Lithos 150, 243–255.

Clemens, J.D., 2003. S-type granitic magmas-petrogenetic issues, models and evidence. Earth-Sci. Rev. 61, 1–18.

Cong, D., Pang, H., Wang, S., Tian, Y., Ying, H., Huang, G., 2019. Zircon LA-ICP-MS U-Pb Ages and the Hf Isotopic Composition of the ore-bearing porphyry from the Yanghuidongzi copper deposit, Heilongjiang, China, and its geological significance. Min. 9 (11), 676.

Corfu, F., Hanchar, J.M., Hoskin, P.W., Kinny, P., 2003. Atlas of zircon textures. Rev. Mineral. Geochem. 53 (1), 469–500.

Dai, B.Z., Jiang, S.Y., Jiang, Y.H., Zhao, K.D., Liu, D.Y., 2008. Geochronology, geochemistry and Hf–Sr–Nd isotopic compositions of Huziyan mafic xenoliths, southern Hunan Province, South China: petrogenesis and implications for lower crust evolution. Lithos 102 (1–2), 65–87.

Deering, C.D., Keller, B., Schoene, B., Bachmann, O., Beane, R., Ovtcharova, M., 2016. Zircon record of the plutonic-volcanic connection and protracted rhyolite melt evolution. Geology 44 (4), 267–270.

Ding, T., Ma, D., Lu, J., Zhang, R., 2015. Apatite in granitoids related to polymetallic mineral deposits in southeastern Hunan Province, Shi-Hang zone, China: Implications for petrogenesis and metallogenesis. Ore Geol. Rev. 69, 104–117.

Doherty, A.L., Webster, J.D., Goldoff, B.A., Piccoli, P.M., 2014. Partitioning behavior of chlorine and fluorine in felsic melt–fluid (s)–apatite systems at 50 MPa and 850–950 °C. Chem. Geol. 384, 94–111.

Dostal, J., Chatterjee, A.K., 2000. Contrasting behaviour of Nb/Ta and Zr/Hf ratios in a peraluminous granitic pluton (Nova Scotia, Canada). Chem. Geol. 163, 207–218.

Ferry, J.M., Watson, E.B., 2007. New thermodynamic models and revised calibrations for the Ti-in-zircon and Zr-in-rutile thermometers. Contrib. Mineral. Petrol. 154 (4), 429–437.

Foster, M. D., 1960. Interpretation of the composition of trioctahedral micas. US Geol. Surv. Prof. Pap., B, 354, 1-49.

Frost, B.R., 1991. Introduction to oxygen fugacity and its petrologic importance. Rev. Mineral. Geochem. 25, 1–9.

Grabezkev, A.I., Vigorova, V.G., Chashukhina, V.A., 1979. Behavior of fluorine during crystallization of granites (in connection with validation of the criteria of granite specialization). Geochem. Int. 16, 23–33.

Gu, X.X., Liu, J.M., Schulz, O., Vavtar, F., Zheng, M.H., 2003. Geochemical constraints on the tectonic setting of the Proterozoic turbidites in the Xuefeng Uplift region of the Jiangnan orogenic belt. Geochem. 32 (5), 406–426 (in Chinese with English abstract).

Hedenquist, J.W., Lowenstern, J.B., 1994. The role of magmas in the formation of hydrothermal ore deposits. Nature 370 (6490), 519–527.

Hemley, J.J., Jones, W.R., 1964. Chemical aspects of hydrothermal alteration with emphasis on hydrogen metasomatism. Econ. Geol. 59, 538–569.

Holtz, F., Dingwell, D.B., Behrens, H., 1993. Effects of F, B_2O_3 and P_2O_5 on the solubility of water in haplogranite melts compared to natural silicate melts. Contrib. Mineral. Petrol. 113 (4), 492–501.

Hoskin, P.W., Schaltegger, U., 2003. The composition of zircon and igneous and metamorphic petrogenesis. Rev. Mineral. Geochem. 53 (1), 27–62.

Huang, L.C., Jiang, S.Y., 2014. Highly fractionated S-type granites from the giant Dahutang tungsten deposit in Jiangnan Orogen, Southeast China: geochronology, petrogenesis and their relationship with W-mineralization. Lithos 202–203 (2014), 207–226.

Jiang, S.Y., Peng, N.J., Huang, L.C., Xu, Y.M., Zhan, G.L., Dan, X.H., 2015. Geological characteristic and ore genesis of the giant tungsten deposits from the Dahutang ore concentrated district in northern Jiangxi Province. Acta Petrol. Sin. 31, 639–655.

Jin, X.B., Wang, L., Xiang, H., Liu, C.P., Duan, G.L., Li, Z.Y., 2017. Petrogenesis of diabase from Jiangshiqiao in Taojiang City, Hu'nan Province: Constrains from geochemistry, geochronology and Sr- Nd- Pb isotopes. Geological Bull. China 36 (5), 750–760 (in Chinese with English abstract).

Keppler, H., 1993. Influence of fluorine on the enrichment of high field strength trace elements in granitic rocks. Contrib. Mineral. Petrol. 114 (4), 479–488.

Keppler, H., 1996. Constraints from partitioning experiments on the composition of subduction-zone fluids. Nature 380 (6571), 237–240.

Keppler, H., Wyllie, P.J., 1991. Partitioning of Cu, Sn, Mo, W, U, and Th between melt and aqueous fluid in the systems haplogranite-H_2O−HCl and haplogranite-H_2O -HF. Contrib. Mineral. Petrol. 109 (2), 139–150.
Kirwin, D.J., 2005. Unidirectional solidification textures associated with intrusion-related Mongolian mineral deposits. In: Seltmann, R., Gerel, O., Kirwin, D.J. (Eds.), Geodynamics and metallogeny of Mongolia with a special emphasis on copper and gold deposits, IAGOD Guidebk Ser. 11, 63–84.
Large, S.J., Quadt, A.V., Wotzlaw, J.F., Guillong, M., Heinrich, C.A., 2018. Magma evolution leading to porphyry Au-Cu mineralization at the Ok Tedi deposit, Papua New Guinea: trace element geochemistry and high-precision geochronology of igneous zircon. Econ. Geol. 113 (1), 39–61.
Li, J., Zhong, J.W., Yu, Y., Huang, X.L., 2013. Insights on magmatism and mineralization from micas in the Xihuashan granite, Jiangxi Province, South China. Geochimica 42 (5), 393–404 (in Chinese with English abstract).
Li, J., Huang, X.L., He, P.L., Li, W.X., Yu, Y., Chen, L.L., 2015. In situ analyses of micas in the Yashan granite, South China: Constraints on magmatic and hydrothermal evolutions of W and Ta–Nb bearing granites. Ore Geol. Rev. 65, 793–810.
Li, X.H., McCulloch, M.T., 1996. Secular variations in Nd isotopic composition of Neoproterozoic sediments from the southern margin of Yangtze block: evidence for a Proterozoic continental collision in southeast China. Precambrian Res. 76, 67–76.
Li, X.Y., Gao, J.F., Zhang, R.Q., Lu, J.J., Chen, W.H., Wu, J.W., 2018. Origin of the Muguayuan veinlet-disseminated tungsten deposit, South China: Constraints from in-situ trace element analyses of scheelite. Ore Geol. Rev. 99, 180–194.
Li, X.Y., Zhang, C., Almeev, R.R., Holtz, F., 2020. GeoBalance: an Excel VBA program for mass balance calculation in geosciences. Geochem. 80, 125629.
Linnen, R.L., Cuney, M., 2005. Granite-related rare-element deposits and experimental constraints on Ta-Nb-W-Sn-Zr-Hf mineralization, in: Linnen, R.L., Samson, I.M. (Eds.), Rare-element geochemistry and mineral deposits.
Loader, M.A., Wilkinson, J.J., Armstrong, R.N., 2017. The effect of titanite crystallisation on Eu and Ce anomalies in zircon and its implications for the assessment of porphyry Cu deposit fertility. Earth Planet Sci. Lett. 472, 107–119.
London, D., 1997. Estimating abundances of volatile and other mobile components in evolved silicic melts through mineral–melt equilibria. J. Petrol. 38 (12), 1691–1706.
Lowenstern, J.B., 1994. Dissolved volatile concentrations in an ore-forming mag- ma. Geology 22 (10), 893–896.
Loucks, R.R., Fiorentini, M.L., Henríquez, G.J., 2020. New magmatic oxybarometer using trace elements in zircon. J. Petrol. Volume 61, Issue 3, March 2020, egaa034, https://doi.org/10.1093/petrology/egaa034.
Luo, S.C., Shu, C.L., 2017. The geological features and relationship of the Muguayuan tungsten-gold deposit in Taojiang, Hunan. Mine. Eng. Constr. 2017 (2), 98–99 (in Chinese with English abstract).
Maaløe, S., Wyllie, P.J., 1975. Water content of a granite magma deduced from the sequence of crystallization determined experimentally with water-undersaturated conditions. Contrib. Mineral. Petrol. 52 (3), 175–191.
Manning, D.A.C., Hill, P.I., 1990. The petrogenetic and metallogenetic significance of topaz granite from the south-west England orefield. Geol. Soc. Amer. Spec. Pap. 246, 51–69.
Mao, J.W., Chen, Y.B., Chen, M.H., Pirajno, F., 2013. Major types and time–space distribution of Mesozoic ore deposits in South China and their geodynamic settings. Miner. Depos. 48 (3), 267–294.
Mao, J.W., Xiong, B.K., Liu, J., Pirajno, F., Cheng, Y.B., Ye, H.S., Song, S.W., Dan, P., 2017. Molybdenite Re-Os dating, zircon U-Pb age and geochemistry of granitoids in the Yangchuling porphyry W-Mo deposit (Jiangnan tungsten ore belt), China: implications for petrogenesis, mineralization and geodynamic setting. Lithos 286–287, 35–52.
Mao, J.W., Ouyang, H.G., Song, S.W., Santosh, M., Yuan, S., Zhou, Z., Zheng, W., Liu, H., Liu, P., Cheng, Y., Chen, M., 2019. Geology and metallogeny of tungsten and tin deposits in China: Society of Economic Geologists. Special Publication 22, 411–482.
Mathez, E.A., Webster, J.D., 2005. Partitioning behavior of chlorine and fluorine in the system apatite-silicate melt-fluid. Geochim. Cosmochim. Acta 69 (5), 1275–1286.
Migdisov, A., Williams-Jones, A.E., Brugger, J., Caporuscio, F.A., 2016. Hydrothermal transport, deposition, and fractionation of the REE: Experimental data and thermodynamic calculations. Chem. Geol. 439, 13–42.
Miller, C.F., McDowell, S.M., Mapes, R.W., 2003. Hot and cold granites? Implications of zircon saturation temperatures and preservation of inheritance. Geology 31 (6), 529–532.
Muhtar, M.N., Wu, C.Z., Brzozowski, M.J., Li, P., Yuan, X.C., Wang, S.M., Zhi, J., Jiang, Y.H., 2020. Geochronology, geochemistry, and Sr–Nd–Pb–Hf–S isotopes of the wall rocks of the Kanggur gold polymetallic deposit, Chinese North Tianshan: implications for petrogenesis and sources of ore-forming materials. Ore Geol. Rev. 125, 103688.
Munoz, J.L., 1984. F-OH and Cl–OH exchange in micas with applications to hydrothermal ore deposits. Rev. Mineral. Geochem. 13, 469–493.
Nabelek, P.I., Bartlett, C.D., 2001. Fertility of metapelites and metagraywackes during leucogranite generation: An example from the Black Hills, USA. Geol. Soc. Amer., Spec. Pap. pp.1-14.
Naney, M.T., 1983. Phase equilibria of rock-forming ferromagnesian silicates in granitic systems. Am. J. Sci. 283 (10), 993–1033.
Nesbitt, H.W., Young, G.M., 1982. Early Proterozoic climates and plate motions inferred from major element chemistry of lutites. Nature 299, 715–717.
Nie, L.Q., Zhou, T.F., White, N., Wang, F.Y., Song, Y.L., 2020. Zircon geochemistry of Edong granitoids in the Middle-Lower Yangtze Metallogenic Belt (Eastern China): Constraints on W-Cu-Fe skarn mineralization. Ore Geol. Rev. 120, 103461.
Pan, L.C., Hu, R.Z., Wang, X.S., Bi, X.W., Zhu, J.J., Li, C.S., 2016. Apatite trace element and halogen compositions as petrogenetic-metallogenic indicators: examples from four granite plutons in the Sanjiang region, SW China. Lithos 254–255, 118–130.
Patiño Douce, A.E., Johnston, A.D., 1991. Phase equilibria and melt productivity in the pelitic system: implications for the origin of peraluminous granitoids and aluminous granulites. Contrib. Mineral. Petrol. 107, 202–218.
Patiño Douce, A.E., Beard, J.S., 1995. Dehydration-melting of biotite gneiss and quartz amphibolite from 3 to 15 kbar. J. Petrol. 36, 707–738.
Pirajno, F., 2009. Intrusion-related hydrothermal mineral systems. In: Hydrothermal Processes and Mineral Systems. Springer, London, pp. 205–259.
Pollard, P.J., Pichavant, M., Charoy, B., 1987. Contrasting evolution of fluorine- and boron-rich tin systems. Miner. Depos. 22 (4), 315–321.
Portnyagin, M., Almeev, R., Matveev, S., Holtz, F., 2008. Experimental evidence for rapid water exchange between melt inclusions in olivine and host magma. Earth Planet Sci. Lett. 272, 541–552.
Putirka, K.D., 2005. Igneous thermometers and barometers based on plagioclase+ liquid equilibria: Tests of some existing models and new calibrations. Am. Mineral. 90 (2–3), 336–346.
Putirka, K.D., 2008. Thermometers and barometers for volcanic systems. Rev. Mineral. Geochem. 69 (1), 61–120.
Pyle, D.M., Mather, T.A., 2009. Halogens in igneous processes and their fluxes to the atmosphere and oceans from volcanic activity: A review. Chem. Geol. 263 (1–4), 110–121.
Rasmussen, K.L., Mortensen, J.K., 2013. Magmatic petrogenesis and the evolution of (F: Cl: OH) fluid composition in barren and tungsten skarn-associated plutons using apatite and biotite compositions: case studies from the northern Canadian cordillera. Ore Geol. Rev. 50, 118–142.
Rickers, K., Thomas, R., Heinrich, W., 2006. The behavior of trace elements during the chemical evolution of the H_2O-, B-, and F-rich granite–pegmatite–hydrothermal system at Ehrenfriedersdorf, Germany: a SXRF study of melt and fluid inclusions. Miner. Depos. 41 (3), 229–245.
Rubatto, D., Hermann, J., 2007. Experimental zircon/melt and zircon/garnet trace element partitioning and implications for the geochronology of crustal rocks. Chem. Geol. 241, 38–61.
Seedorff, E., Dilles, J.H., Proffett, Jr., J.M., Einaudi, M.T., Zurcher, L., Stavast, W.J.A., Johnson, D.A., Barton, M.D., 2005. Porphyry deposits: Characteristics and origin of hypogene features. Econ. Geol. 100th Annv. 251–298.
Sha, L.K., Chappell, B.W., 1999. Apatite chemical composition, determined by electron microprobe and laser-ablation inductively coupled plasma mass spectrometry, as a probe into granite petrogenesis. Geochim. Cosmochim. Acta 63, 3861–3881.
Shan, L., Pang, Y.C., Ke, Z.X., Liu, J.J., Chen, W.H., Niu, Z.J., Xu, D.M., Long, W.G., Wang, B.Q., 2019. Diagenetic and metallogenic age of the Muguayuan tungsten polymetallic deposit and its effect on regional mineralization, Taojiang County, northeastern Hunan Province, China. Geol. Sci. Technol. Information 38, 100–112 (in Chinese with English abstract).
Shaw, D.M., 1970. Trace element fractionation during anatexis. Geochim. Cosmochim. Acta 34 (2), 237–243.
Sillitoe, R.H., 2010. Porphyry copper systems. Econ. Geol. 105, 3–41.
Simons, B., Shail, R.K., Andersen, J.C., 2016. The petrogenesis of the Early Permian Variscan granites of the Cornubian Batholith: lower plate post-collisional peraluminous magmatism in the Rhenohercynian Zone of SW England. Lithos 260, 76–94.
Sinclair, W.D., Gonevchuk, G.A., Korostelev, P.G., Semenyak, B.I., Rodionov, S., Seltmann, R., Štemprok, M., 2011. World distribution of tin and tungsten deposits. Geological Survey of Canada, Open File 5482, scale 1: 35,000,000.
Skjerlie, K.P., Johnston, A.D., 1996. Vapour-absent melting from 10 to 20 kbar of crustal rocks that contain multiple hydrous phases: implications for anatexis in the deep to very deep continental crust and active continental margins. J. Petrol. 37, 661–691.
Sparks, R.S.J., Barclay, J., Jaupart, C., Mader, H.M., Phillips, J.C., 1994. Physical aspects of magma degassing, 1, Experimental and theoretical constraints on vesiculation, in Carroll, M.R., Holloway, J.R. (Eds.), Volatiles in Magmas, Mineral. Soc. of Am., Washington, DC. pp. 413–445.
Štemprok, M., 1990. Solubility of tin, tungsten and molybdenum oxides in felsic magmas. Miner. Depos. 25 (3), 205–212.
Stepanov, A.S., Mavrogenes, J., Meffre, S., Davidson, P., 2014. The key role of mica during igneous concentration of tantalum. Contrib. Mineral. Petrol. 167 (6), 1009.
Stussi, J.M., Cuney, M., 1996. Nature of biotites from alkaline, calc-alkaline and peraluminous magmas by Abdel-Fattah M. Abdel-Rahman: a comment. J. Petrol. 37, 1025–1029.
Sun, K.K., Chen, B., 2017. Trace elements and Sr-Nd isotopes of scheelite: Implications for the W-Cu-Mo polymetallic mineralization of the Shimensi deposit, South China. Am. Mineral. 102 (5), 1114–1128.
Sun, S., Mcdonough, W.F., 1989. Chemical and isotopic systematics of oceanic basalts: implications for mantle composition and processes. Geol. Soc. Lond., Spec. Publ. 42 (1), 313–345.
Sylvester, P.J., 1998. Post-collisional strongly peraluminous granites. Lithos 45 (1), 29–44.
Tang, Y.M., Zhao, Q.H., Luo, S.C., 2016. Geological charactertics and metallogenetic regularity of the Muguayuan porphyry tungsten deposit in Taojiang, Hunan. Western Resour. 3, 94–95 (in Chinese).
Teiber, H., Marks, M.A., Wenzel, T., Siebel, W., Altherr, R., Markl, G., 2014. The distribution of halogens (F, Cl, Br) in granitoid rocks. Chem. Geol. 374, 92–109.
Tindle, A.G., Webb, P.C., 1990. Estimation of lithium contents in trioctahedral micas using microprobe data: application to micas from granitic rocks. Eur. J. Mineral. 595–610.
Timofeev, A., Migdisov, A.A., Williams-Jones, A.E., 2017. An experimental study of the solubility and speciation of tantalum in fluoride-bearing aqueous solutions at elevated temperature. Geochim. Cosmochim. Acta 197, 294–304.

Timofeev, A., Williams-Jones, A.E., 2015. The origin of niobium and tantalum mineralization in the Nechalacho REE Deposit, NWT. Canada. Econ. Geol. 110 (7), 1719–1735.
Trail, D., Watson, E.B., Tailby, N.D., 2012. Ce and Eu anomalies in zircon as proxies for the oxidation state of magmas. Geochim. Cosmochim. Acta 97, 70–87.
Tsay, A., Zajacz, Z., Sanchez-Valle, C., 2014. Efficient mobilization and fractionation of rare-earth elements by aqueous fluids upon slab dehydration. Earth Planet Sci. Lett. 398, 101–112.
Villemant, B., Boudon, G., 1999. H_2O and halogen (F, Cl, Br) behaviour during shallow magma degassing processes. Earth Planet Sci. Lett. 168 (3–4), 271–286.
Wang, W., Wang, F., Chen, F., Zhu, X., Xiao, P., Siebel, W., 2010. Detrital zircon ages and Hf-Nd isotopic composition of neoproterozoic sedimentary rocks in the Yangtze Block: constraints on the deposition age and provenance. J. Geol. 118 (1), 79–94.
Wang, X.L., Zhou, J.C., Qiu, J.S., Gao, J.F., 2004. Geochemistry of the Meso- to Neoproterozoic basic-acid rocks from Hunan Province, South China: implications for the evolution of the western Jiangnan orogeny. Precambrian Res. 133, 17–103.
Wang, X.L., Zhou, J.C., Griffin, W.L., Wang, R.C., Qiu, J.S., Oreilly, S.Y.O., Xu, X.S., Liu, X.M., Zhang, G.L., 2007a. Detrital zircon geochronology of Precambrian basement sequences in the Jiangnan Orogen: dating the assembly of the Yangtze and Cathaysia Blocks. Precambrian Res. 159 (1), 117–131.
Wang, Y.J., Fan, W.M., Sun, M., Liang, X.Q., Zhang, Y.H., Peng, T.P., 2007b. Geochronological, geochemical and geothermal constraints on petrogenesis of the Indosinian peraluminous granites in the south china block: a case study in the Hunan Province. Lithos 96 (3–4), 475–502.
Wang, Y.Y., Kerkhof, A.V.D., Xiao, Y.L., Sun, H., Yang, X.Y., Lai, J.Q., Wang, Y.G., 2017. Geochemistry and fluid inclusions of scheelite-mineralized granodiorite porphyries from southern Anhui Province. China. Ore Geol. Rev. 89, 988–1005.
Waters, L.E., Lange, R.A., 2015. An updated calibration of the plagioclase-liquid hygrometer-thermometer applicable to basalts through rhyolites. Am. Mineral. 100 (10), 2172–2184.
Watson, E.B., 1996. Dissolution, growth and survival of zircons during crustal fusion: kinetic principals, geological models and implications for isotopic inheritance. Trans. R. Soc. Edinburgh-Earth Sci. 87 (1), 43–56.
Watson, E.B., Harrison, T.M., 1983. Zircon saturation revisited: temperature and composition effects in a variety of crustal magma types. Earth Planet Sci. Lett. 64 (2), 295–304.
Webster, J., Thomas, R., Förster, H.-J., Seltmann, R., Tappen, C., 2004. Geochemical evolution of halogen-enriched granite magmas and mineralizing fluids of the Zinnwald tin-tungsten mining district, Erzgebirge, Germany. Miner. Depos. 39 (4), 452–472.
Webster, J.D., Thomas, R., Rhede, D., Seltmann, R., Förster, H.J., Veksler, I., 1998. Late-stage processes in P-or F-rich granitic magmas. Acta Universitatis Carolinae: Geologica 42 (1), 181–188.
Webster, J.D., Rebbert, C.R., 2001. The geochemical signature of fluid-saturated magma determined from silicate melt inclusions in Ascension Island granite xenoliths. Geochim. Cosmochim. Acta 65 (1), 123–136.
Webster, J.D., 1992. Fluid-melt interactions involving Cl-rich granites: Experimental study from 2 to 8 kbar. Geochim. Cosmochim. Acta 56, 679–687.
Webster, J.D., 1997. Exsolution of Cl-bearing fluids from chlorine-enriched mineralizing granitic magmas and implications for ore metal transport. Geochim. Cosmochim. Acta 61, 1017–1030.
Wilkinson, J.J., 2001. Fluid inclusions in hydrothermal ore deposits. Lithos 55 (1), 229–272.
Williams-Jones, A.E., Migdisov, A.A., 2014. Experimental constraints on the transport and deposition of metals in ore-forming hydrothermal systems. Econ. Geol. 18, 77–96.
Winter, J.D., 2012. Principles of Igneous and Metamorphic Petrology. Pearson education, Harlow, UK, pp. 38–40.
Wu, F.Y., Jahn, B.M., Wilde, S.A., Lo, C.H., Yui, T.F., Lin, Q., Ge, W.C., Sun, D.Y., 2003. Highly fractionated I-type granites in NE China (I): geochronology and petrogenesis. Lithos 66 (3), 241–273.
Wu, F.Y., Liu, X.C., Ji, W.Q., Wang, J.M., Yang, L., 2017. Highly fractionated granites: Recognition and research. Sci. China Earth Sci. 60, 1201–1219.
Xie, G.Q., Mao, J.W., Bagas, L., Fu, B., Zhang, Z., 2018a. Mineralogy and titanite geochronology of the Caojiaba W deposit, Xiangzhong metallogenic province, southern China: implications for a distal reduced skarn W formation. Miner. Depos. 54 (3), 459–472.
Xie, G.Q., Mao, J.W., Li, W., Fu, B., Zhang, Z., 2018b. Granite-related Yangjiashan tungsten deposit, southern China. Miner. Depos. 54 (1), 67–80.
Xu, D.R., Gu, X.X., Li, P.C., Chen, G.H., Xia, B., Bachlinski, R., He, Z.L., Fu, G.G., 2007. Mesoproterozoic-Neoproterozoic transition: Geochemistry, provenance and tectonic setting of clastic sedimentary rocks on the SE margin of the Yangtze Block, South China. J. Asian Earth Sci. 29, 637–650.
Yang, X., 1992. Source of ore material and paragenesis of ore-building elements in Woxi Au-Sb-W deposit, Hunan. J. Chengdu College Geol. 19 (2), 20–28 (in Chinese).
Zajacz, Z., Halter, W.E., Pettke, T., Guillong, M., 2008. Determination of fluid/melt partition coefficients by LA-ICPMS analysis of co-existing fluid and silicate melt inclusions: controls on element partitioning. Geochim. Cosmochim. Acta 72 (8), 2169–2197.
Zhang, L.S., 2013. Skarn and ore Genesis of the Darongxi Tungsten Deposit, Western Hunan. Master thesis of. Central South University, Hunan.
Zhang, Q., Zhang, R.Q., Gao, J.F., Lu, J.J., Wu, J.W., 2018. In-situ LA-ICP-MS trace element analyses of scheelite and wolframite: Constraints on the genesis of veinlet-disseminated and vein-type tungsten deposits. South China. Ore Geol. Rev. 99, 166–179.
Zhang, W., Lentz, D.R., Thorne, K.G., McFarlane, C., 2016. Geochemical characteristics of biotite from felsic intrusive rocks around the Sisson Brook W-Mo–Cu deposit, west-central New Brunswick: an indicator of halogen and oxygen fugacity of magmatic systems. Ore Geol. Rev. 77, 82–96.
Zhang, S.T., Zhang, R.Q., Lu, J.J., Ma, D.S., Ding, T., Gao, S.Y., Zhang, Q., 2019. Neoproterozoic tin mineralization in South China: geology and cassiterite U-Pb age of the Baotan tin deposit in northern Guangxi. Miner. Depos. 54 (8), 1125–1142.
Zhang, Y., Yang, J.H., Chen, J.Y., Wang, H., Xiang, Y.X., 2017. Petrogenesis of Jurassic tungsten-bearing granites in the Nanling Range, South China: Evidence from whole-rock geochemistry and zircon U-Pb and Hf–O isotopes. Lithos 278–281, 166–180.
Zhao, W.W., Zhou, M.F., Li, Y.H.M., Zhao, Z., Gao, J.F., 2017a. Genetic types, mineralization styles, and geodynamic settings of Mesozoic tungsten deposits in South China. J. Asian Earth Sci. 137, 109–140.
Zhao, Z.X., Miao, B.H., Xu, Z.W., Lu, J.J., Liu, L., Zuo, C.H., Lu, R., Wang, H., 2017b. Petrogenesis of two types of Late Triassic granite from the Guandimiao Complex, southern Hunan Province, China. Lithos 282–283, 403–419.